Journal of Nanobiotechnology

RESEARCH Open Access

Adipose-derived small extracellular vesicle miR-146a-5p targets Fbx32 to regulate mitochondrial autophagy and delay aging in skeletal muscle

Mengran Qin[1,2,3,4†], Yan Wang[1,2,3†], Zihan Wang[5], Benchao Dong[1,2,3], Peichuan Yang[1,2,3], Youyi Liu[1,2,3,5], Qianyun Xi[4*] and Jianxiong Ma[1,2,3*]

Abstract

This study investigates how miR-146a-5p, found in adipose tissue-derived small extracellular vesicles (sEV), influences mitochondrial autophagy and its impact on delaying skeletal muscle aging through the targeting of Fbx32. The findings highlight miR-146a-5p as crucial in skeletal muscle development and aging, influencing autophagy, apoptosis, differentiation, and proliferation, collectively impacting muscle atrophy. In C2C12 cells, miR-146a-5p mimics decreased apoptosis, autophagy, and reactive oxygen species (ROS) levels, while enhancing ATP production; conversely, miR-146a-5p inhibitors had the opposite effects. Furthermore, miR-146a-5p-enriched sEV from adipose tissue alleviated skeletal muscle atrophy in aged mice and promoted muscle fiber growth and repair by regulating mitochondrial autophagy and apoptosis. Mechanistically, miR-146a-5p modulated mitochondrial autophagy in myoblasts by targeting Fbx32 and impacting the FoxO3 signaling pathway. This led to a notable decrease in apoptosis-related gene expression, reduced ROS production, and elevated ATP levels. In conclusion, miR-146a-5p derived from WAT-sEV modulates myoblast autophagy, apoptosis, ROS, and differentiation through the Fbx32/FoxO3 signaling axis. This work presents a novel molecular target and theoretical framework for delaying skeletal muscle aging and developing therapies for skeletal muscle-related disorders.

Keywords sEV, miR-146a-5p, Fbx32, Mitochondrial autophagy, Aging

†Mengran Qin and Yan Wang contributed equally to this work.

*Correspondence:
Qianyun Xi
xqy0228@scau.edu.cn
Jianxiong Ma
yjslwtg@126.com
[1]Tianjin Hospital, Tianjin University, Tianjin 300211, China
[2]Tianjin Orthopedic Institute, Tianjin 300050, China
[3]Tianjin Key Laboratory of Orthopedic Biomechanics and Medical Engineering, Tianjin 300050, China
[4]College of Animal Science, Guangdong Province Key Laboratory of Animal Nutritional Regulation, National Engineering Research Center for Breeding Swine Industry, State Key Laboratory of Livestock and Poultry Breeding, South China Agricultural University, Guangzhou 510642, Guangdong, China
[5]Tianjin Key Laboratory of Agricultural Animal Breeding and Healthy Husbandry, College of Animal Science and Veterinary Medicine, Tianjin Agricultural University, Tianjin 300392, China

Introduction

Adipose tissue functions as a vital energy reserve and endocrine organ, influencing metabolic regulation in various organs, including skeletal muscle. This is accomplished through the secretion of sEV, which carries microRNA (miRNAs) and other regulatory molecules. These vesicles facilitate intercellular communication by entering target cells through endocytosis, membrane fusion, or receptor-mediated mechanisms, significantly contributing to the interaction between adipose tissue and skeletal muscle [1–3]. sEV influences adipose tissue and skeletal muscle functions through complex interactions [4, 5]. Skeletal muscle wasting is a common consequence of conditions such as fasting, aging, cancer, diabetes, sepsis, renal failure, and denervation [6, 7]. F-box protein 32 (Fbx32), or Atrogin-1, is a crucial E3 ubiquitin ligase involved in muscle protein degradation and significantly contributes to muscle atrophy. FoxO3 transcription factor controls the expression of Fbx32 [8]. Increased Fbx32 levels accelerate protein degradation and promote muscle atrophy by enhancing mitochondrial autophagy, which is essential for maintaining muscle cell function [9–11]. Age-related mitochondrial dysfunction is a key contributor to skeletal muscle wasting.

miRNAs are a class of small non-coding RNA molecules that play a key role in controlling gene expression [12]. Prior studies indicate that miR-146a-5p, transported via sEV from skeletal muscle, affects the PPARγ signaling pathway by targeting GDF5, thus suppressing adipogenesis [13]. Similarly, Yu et al. Research has shown that skeletal muscle cells can absorb miR-27a from adipose-derived sEV [14]. Despite these insights, the role of adipose-derived sEV and their mechanisms in adipose-skeletal muscle communication remain underexplored. This research investigates miR-146a-5p's influence on mitochondrial autophagy in skeletal muscle via adipose-derived sEV, utilizing both cellular and animal models. Our findings reveal that miR-146a-5p inhibits mitochondrial autophagy by downregulating Fbx32 expression, ultimately slowing skeletal muscle atrophy. This research investigates the molecular interactions between adipose tissue and skeletal muscle, providing a foundation for understanding the regulatory mechanisms of muscle aging.

Materials and methods

Animals

Animals for the study were sourced from a commercial farm in Xinfeng County, Shaoguan City, Guangdong Province, China. A total of 20 male pigs were selected, including 5 lean-type piglets (LR) and 5 Chinese fat-type piglets (LT) at 1 day of age, as well as 5 lean-type pigs (CS) at 60 and 90 days of age. Adipose tissue and samples from the longest dorsal muscle were swiftly harvested and preserved in liquid nitrogen for future analysis.

Adipose-specific miR-146a-5p knockout (aKO) mice were created utilizing the Cre-loxP system (Cyagen, Suzhou, China). The breeding process involved crossing miR-146a-5p flox/flox (miR-146a-5p $flox^{+/+}$, Flox) mice with adipose tissue-specific Cre mice. The resulting F1 generation (miR-146a-5p $flox^{+/-}$, $Cre^{+/-}$) was then bred with miR-146a-5p $flox^{+/+}$ mice to generate aKO (miR-146a-5p $flox^{+/+}$, $Cre^{+/-}$) and control Flox (miR-146a-5p $flox^{+/+}$) mice. The mice were housed in individually ventilated cages under pathogen-free conditions at 24℃, maintained on a 12-hour light/dark cycle, and provided with a standard diet from the Tianjin Hospital Animal Experiment Center (Tianjin, China). The study predominantly used male mice aged 8 to 12 weeks, with additional groups of younger (4 weeks) and older (18 months) mice for specific analyses. All experimental procedures complied with the National Institutes of Health guidelines for laboratory animal care and use and were approved by the Tianjin Hospital Animal Research Ethics Committee (Ethical approval number: 2024YLS208).

Immunofluorescence

Muscle tissue samples were rapidly frozen in isopentane cooled with liquid nitrogen and embedded in Tissue-Tek OCT (Fisher Scientific/Thermo Scientific). Cryosections, 10 μm thick, were prepared at -25℃ and fixed with 4% paraformaldehyde for 10 min. The sections underwent three 5-minute washes with PBS, followed by blocking with a solution containing PBS, 0.5 mL goat serum, 0.2 g BSA, 0.2 mL 10% Triton X-100, and 0.01 g sodium azide. Primary antibodies were incubated overnight at 4 °C, comprising mouse anti-MyoD (1:100, Santa Cruz, sc-377460), rabbit anti-laminin (1:1000, Thermo Fisher, PA1-16730), mouse anti-MyHC (1:2000, R&D Systems, MAB4470), and mouse anti-Pax7 (1:50, DSHB, 528428). Following three PBS washes, the sections were incubated at room temperature for 1 h with secondary antibodies: goat anti-mouse IgM/Alexa Fluor 555 (1:2000, bs-0368G-AF555, Bioss) and goat anti-rabbit FITC (1:2000, bs-0295G-FITC, Bioss). To minimize background staining, the sections were treated with 0.05% Sudan black for 5 min. Fluorescent images were obtained using a Nikon Eclipse Ti inverted microscope (Tokyo, Japan).

C2C12 cells were fixed with 4% paraformaldehyde and permeabilized with 0.4% Triton X-100 in PBS, each for 20 min at room temperature. Cells were initially blocked with 5% goat serum for 1 h and then incubated overnight at 4℃ with primary antibodies: anti-MyoD (sc-377460, Santa Cruz), anti-MyHC (MAB4470, R&D Systems), and anti-Pax7 (528428, DSHB). The cells were then incubated in the dark at room temperature for 1 h with goat anti-mouse IgM conjugated to Alexa Fluor 555 (1:2000,

bs-0368G-AF555, Bioss). Nuclei were DAPI-stained. Fluorescent images were acquired with a Nikon Eclipse Ti microscope, and myotube diameters were quantified using ImageJ software.

Skeletal muscle satellite cell extraction and culturing

Muscles from both mice and piglets were used as tissue sources for isolating skeletal muscle satellite cells (MuSCs). Mice, approximately 10 days old, were euthanized by cervical dislocation and processed under aseptic conditions. After sterilizing the mice in 75% ethanol, the hind limb skin was carefully removed, and blood vessels, connective tissue, fat, and bone were discarded, leaving only the muscle tissue. For piglets, euthanasia was performed via cardiac puncture, and the longissimus dorsi muscle was aseptically isolated. The muscle tissue was then washed with PBS until the rinse solution was clear, and it was minced into approximately 1 mm^3 pieces. The minced muscle was incubated in 0.2% collagenase II at 37℃ for 1 h in a water bath shaker, with gentle agitation every 10 min. Post-digestion, the mixture was centrifuged at 1000 rpm for 10 min at 4℃, and the supernatant was removed. The pellet was treated with 0.25% trypsin at 37 °C for 30 min, with agitation every 10 min. Trypsin activity was inhibited by adding a growth medium containing 20% fetal bovine serum (FBS) and 1% penicillin-streptomycin (P/S) (Gibco). The cell suspension was filtered through 100, 200, and 400 mesh filters in sequence, then centrifuged at 1000 rpm for 10 min at 4℃. The pellet was resuspended in fresh growth medium and transferred to 25 cm^2 culture flasks after the supernatant was discarded. The cells were incubated at 37℃ in a 5% CO_2 environment. To purify MuSC, a differential apposition technique was used. The isolated muscle cells were incubated for two hours, enabling fibroblasts to attach to the surface while the satellite cells remained in suspension. Non-adherent cells were moved to new culture flasks, and on day 4, the medium was changed to eliminate residual blood and dead cells. Cell growth was monitored, and cells were passaged upon reaching 75-90% confluence. At each passaging, a 30-minute differential walling was performed to further eliminate fibroblasts.

Cell culture

C2C12 myoblasts were maintained in 12-well plates (Corning) with high-glucose DMEM (Gibco), supplemented with 10% FBS and 1% P/S. Upon reaching confluence, the culture medium was replaced with a differentiation medium containing DMEM and 2% horse serum (HS, Gibco) for a 6-day induction period. Replace the medium every two days. MuSCs or C2C12 cells were seeded at 1×10^5 cells per well in 12-well plates for transfection experiments. Cells at 60–70% confluence were exposed to 40 nM miR-146a-5p mimics, 80 nM miR-146a-5p inhibitor, 50 nM si-Fbx32 or 10 μg/mL sEV. Transfection utilized siRNAs from GenePharma and Tsingke Biological Technology, China, in conjunction with Lipofectamine 2000 (Thermo Fisher), adhering to the manufacturer's guidelines.

CCK-8 assay

Cells were seeded in a 96-well plate and treated according to the experimental design. After incubation, Cell Counting Kit-8 (CCK-8) solution was added to each well, and the plate was further incubated. Absorbance was measured at 450 nm using a microplate reader to determine cell viability. Cell viability was evaluated with the CCK-8 assay. C2C12 cells were plated in 96-well plates at a density of 10,000 cells per well, with six replicates per condition. Following treatment, each well received 10 μL of CCK-8 reagent and 90 μL of the medium mix, then incubated for 1 h. Absorbance at 450 nm was measured using a BioTek microplate reader, with blank wells as controls. Cell viability and proliferation were assessed following the manufacturer's guidelines (Beyotime, Haimen, China).

EdU incorporation assay

Cell proliferation was evaluated using the BeyoClick™ EdU Cell Proliferation Kit with Alexa Fluor 488 (Beyotime, C0071) according to the manufacturer's protocol. C2C12 cells were plated in 96-well plates at a density of 1.0×10^4 cells per well and incubated with 10 μM EdU for 2 h at 37℃ in a CO_2 incubator. Following incubation, the cells were fixed in 4% paraformaldehyde for 20 min, then permeabilized with 0.3% Triton X-100 for 15 min. The Click Reaction Mixture was incubated at room temperature in the dark for 30 min, then stained with Hoechst 33,342 for 10 min. EdU-positive cells were quantified using ImageJ software [15].

Flow cytometric analysis of cell apoptosis

Apoptosis was assessed via flow cytometry (BD FACSCalibur) using the Annexin V-FITC/PI Apoptosis Detection Kit (BD Biosciences). Cells were first harvested by trypsinization and transferred into 15 mL centrifuge tubes. After centrifuging at 1,000 g for 5 min, the supernatant was discarded, and the cell pellet was washed twice with cold PBS. Following each wash, the cells were re-centrifuged, resuspended in PBS, and counted to ensure the correct concentration. For apoptosis analysis, 50,000 to 100,000 cells underwent additional centrifugation, followed by supernatant removal. The pellet was resuspended in 500 μL of Annexin V binding buffer, then 5 μL of Annexin V-FITC and 5 μL of propidium iodide (PI) were added. The mixture was gently vortexed and left to incubate in the dark at room temperature (20–25℃)

for 15 min. Apoptosis levels were assessed post-incubation via flow cytometry, allowing for the distinction of early apoptotic, late apoptotic, and necrotic cells.

Transmission Electron microscopy

Mice were humanely euthanized and perfused with 100 mM sodium phosphate buffer (pH 7.4). The tissues were immersed in a phosphate buffer (PB) fixative containing 2.5% glutaraldehyde and 1% paraformaldehyde. The tibialis anterior (TA) muscle was carefully dissected, cut into smaller pieces, and stored overnight in the same fixative at 4℃. After a PB rinse, samples were incubated in 0.2 M imidazole for 15 min and subsequently fixed with 1% osmium tetroxide. Following an additional rinse with high-purity water, the samples were incubated overnight at 4℃ in a 1% aqueous lead nitrate solution. A series of graded acetone solutions were employed for dehydration, and the samples were subsequently embedded in epoxy resin at a temperature of 60℃ for 24 h. Ultra-thin sections were then prepared using an ultramicrotome, placed on copper grids, and examined with a transmission electron microscope under conditions of double-blind analysis [16].

sEV isolation, characterization, and administration

sEV were isolated from the white adipose tissue of 3-month-old mice. The tissue was rinsed thrice with PBS and cut into pieces under 3 mm. The culture was kept in 75 cm^2 flasks containing 25 mL of DMEM, with the addition of 1% P/S and 10% sEV-depleted FBS, for 24 h at 37℃. After incubation, the supernatant was centrifuged in stages: first at 300×g for 10 min to remove suspended cells, then at 2,000×g for 10 min to eliminate dead cells, and finally at 10,000×g for 30 min to clear cellular debris. The supernatant was concentrated using a 100 kDa protein concentrator (Macrosep) and subsequently purified with a 0.22 μm PVDF filter (Millipore). The concentrated sample underwent ultracentrifugation at 120,000×g for 90 min using a 38.5 mL Beckman Coulter tube. After ultracentrifugation, the sEV were washed with PBS, resuspended, and aliquoted into 100 μL portions in PBS for storage at -80℃. The sEV isolated from the white adipose tissue (WAT) of Flox and aKO mice were labeled as Flox-sEV and aKO-sEV, respectively.

Western blot analysis was conducted to characterize the sEV using extracellular vesicle markers TSG101, Alix, CD9, and CD63, with Calnexin serving as a negative control for the endoplasmic reticulum. The concentration and size distribution of sEV were evaluated using a Nanosight instrument, and their morphology was analyzed through transmission electron microscopy (TEM) [17].

For in vivo administration, recipient mice received three weekly injections of 100 μg sEV into the TA muscle. In vitro, cells were treated with sEV at a concentration of 10 μg/mL. The uptake of sEV was tracked by labeling the vesicles with PKH67 fluorescent dye, as per the manufacturer's guidelines (Sigma-Aldrich).

Dual-Luciferase reporter assay

To evaluate gene expression, a dual-luciferase reporter assay was performed. HEK293T cells were cultured in 96-well plates (Corning) at a density of 2.5×10^4 cells per well and allowed to reach 60-70% confluence. Cells were co-transfected with 100 ng of a dual-luciferase reporter plasmid (containing wild-type, mutant, or deleted target sequences) and 3 pmol of either the miR-146a-5p mimic or a negative control. After 24 h of incubation, luciferase activities were measured using the Dual-GLO luciferase assay system (Promega), following the manufacturer's instructions. Firefly luciferase activity was normalized to Renilla luciferase activity to correct for transfection efficiency [18].

Detection of reactive oxygen species (ROS)

Intracellular ROS levels in C2C12 cells were measured using the ROS assay kit (S0033, Beyotime, Shanghai, China) according to the manufacturer's instructions. Fluorescent emissions were visualized and documented using a fluorescence microscope.

Cellular ATP level analysis

ATP levels in cell lysates were quantified using the ATP assay kit (Beyotime, Cat# S0026). A 20 μL aliquot of lysate was mixed with 10 μL of ATP detection reagent, and luminescence was measured using a BioTek microplate reader. Protein concentrations were measured using the Pierce BCA assay kit. ATP levels were then normalized to the protein content for calculation.

Quantitative Real-Time PCR

Total RNA was extracted following the manufacturer's protocol using TRIzol reagent (Thermo Fisher). To remove genomic DNA contamination, RNA samples underwent treatment with DNase I (EZB, Shanghai, China). cDNA was synthesized by reverse transcribing 1–2 μg of RNA using the EZB 4×EZscript Reverse Transcription Mix II (EZB, Shanghai, China). Quantitative real-time PCR (qPCR) was performed on the Bio-Rad C1000 Touch (QuantStudio Real-Time PCR System) with the 2×RealStar Fast SYBR qPCR Mix (GenStar, Cat No. A301), as per the manufacturer's guidelines. GAPDH served as the internal control for mRNA quantification, while U6 RNA was used to normalize miRNA expression levels. The 2-ΔΔCt method was used to quantify relative mRNA levels [19].

Western blotting

The expression of various functional proteins was evaluated using Western blotting. Protein samples were lysed using RIPA buffer and quantified with Thermo Fisher's Rapid Gold BCA Protein Assay Kit. Each sample's 15 μg protein underwent SDS-PAGE and was transferred to PVDF membranes (Millipore) for analysis. Primary antibodies included anti-TSG101 (rabbit, ZEN BIO, 381538), anti-Alix (rabbit, Sangon Biotech, D262028), anti-Calnexin (rabbit, Sangon Biotech, D262986), anti-CD63 (rabbit, Sangon Biotech, D160973), anti-Wnt 10b (rabbit, Bioss, bs-3662R), anti-CD9 (rabbit, Abcepta, AP68-965), anti-Cyclin A2 (rabbit, GeneTex, GTX103042), anti-Cyclin D1 (rabbit, CST, 2978 S), anti-Cyclin E1 (rabbit, ZEN BIO, 340298), anti-PCNA (mouse, ZEN BIO, 200947), anti-MyHC (mouse, R&D Systems, MAB4470), anti-MyoD (rabbit, ZEN BIO, 252249), anti-MyoG (rabbit, ZEN BIO, 382257), anti-Fbx32 (rabbit, Abclonal, A3193), anti-MuRF (rabbit, Abclonal, A3101), anti-Pax7 (rabbit, Abclonal, A7335), anti-Bcl-2 (rabbit, ZEN BIO, 380709), anti-Bax (rabbit, Sangon Biotech, D290151), anti-Caspase 3 (rabbit, ZEN BIO, 300968), anti-LC3 (mouse, abcam, ab243506), anti-P62 (rabbit, Abclonal, A19700), and anti-Tubulin (rabbit, Bioworld, AP0064). The membrane was incubated with the primary antibody overnight, followed by a one-hour exposure to the secondary antibody (Bioworld) at room temperature. Protein bands were visualized by a gel imaging system and normalized using Tubulin as an internal control. Quantitative results of protein bands were expressed in arbitrary units (AU) relative to the control. Data analysis was conducted using ImageJ software [20].

Statistical analysis

Statistical analyses, comprising one-way ANOVA, independent t-tests, and data visualization, were conducted using SPSS (v27) and GraphPad Prism (v9.0). Data are presented as means ± standard error of the mean (SEM). Groups were compared using either an unpaired Student's t-test or one-way ANOVA for statistical analysis. Statistical significance was defined as $^{*}P < 0.05$ and $^{**}P < 0.01$. The letters a, b, and c denote varying significance levels between groups; distinct letters indicate a significant difference, while identical letters imply no significant difference [21].

Results

Expression of miR-146a-5p in pig skeletal muscle tissues and skeletal muscle development characteristics

The formation and development of skeletal muscles in pigs is a highly intricate process, with notable variations in growth rates and meat quality across various pig breeds. Skeletal muscle fiber growth and development are impacted by various factors, with breed and age being key contributors. This study examined miR-146a-5p expression in adipose and skeletal muscle tissues and investigated gene expression differences associated with skeletal muscle development in 1-day-old Chinese fat-type Langtang (LT) and lean-type Landrace (LR) piglets. The findings indicated that miR-146a-5p expression levels in the fat and skeletal muscle of LR piglets were notably greater than those in LT piglets (Fig. 1a). Western blot analysis showed a significant reduction in the expression of cell proliferation-related proteins, such as Cyclin A2, Cyclin D1, Cyclin E1, and PCNA, in the skeletal muscle of LR piglets compared to LT piglets (Fig. 1b-c). RT-qPCR and Western Blot were simultaneously employed to assess mRNA and protein expression of genes associated with skeletal muscle differentiation. Additionally, mRNA and protein expression of MyoG and MyoD significantly increased, along with a notable rise in MyHC protein levels. The skeletal muscle of LR piglets exhibited a significant reduction in Fbx32 and MuRF expression (Fig. 1d-f). This study analyzed miR-146a-5p expression and changes in skeletal muscle development-related genes in 1-day-old lean-type LR piglets, 60-day-old lean-type ternary hybrid (CS) pigs, and 90-day-old CS pigs. The findings indicated that LR piglets had the highest miR-146a-5p expression compared to the other pig groups, whereas 90-day-old CS pigs had the lowest expression (Fig. 1g). RT-qPCR analysis indicated that in 90-day-old CS pigs, there was a significant down-regulation of MyoD and MyoG mRNA levels, alongside a significant up-regulation of Fbx32 and MuRF levels (Fig. 1h). Western blot analysis confirmed a marked decrease in MyoG, MyoD, and MyHC protein levels in 90-day-old CS pigs. In contrast, the protein levels of Fbx32 and MuRF were markedly elevated (Fig. 1i-j). miR-146a-5p expression is significantly linked to skeletal muscle development in pigs, with notable differences across breeds and ages.

Expression and developmental characteristics of miR-146a-5p in mouse skeletal muscle tissue

The study examined miR-146a-5p's impact on skeletal muscle growth in both young and aged wild-type mice. Examination of TA muscle sections revealed that aged mice exhibited an increase in smaller skeletal muscle fiber areas (0–200 μm^2) and a notable reduction in larger fiber areas (1000–3000 μm^2) compared to young mice (Fig. 2a-b). RT-qPCR analysis revealed significantly reduced miR-146a-5p expression in the skeletal muscles of aged mice compared to young mice (Fig. 2c). Western blot analysis demonstrated a notable increase in proliferation-related proteins, such as PCNA, Cyclin D1, Cyclin A2, and Cyclin E1, in the skeletal muscles of aged mice relative to young mice (Fig. 2d-e). RT-qPCR and Western Blot analyses revealed a significant decline in MyHC protein levels, along with reduced mRNA expression

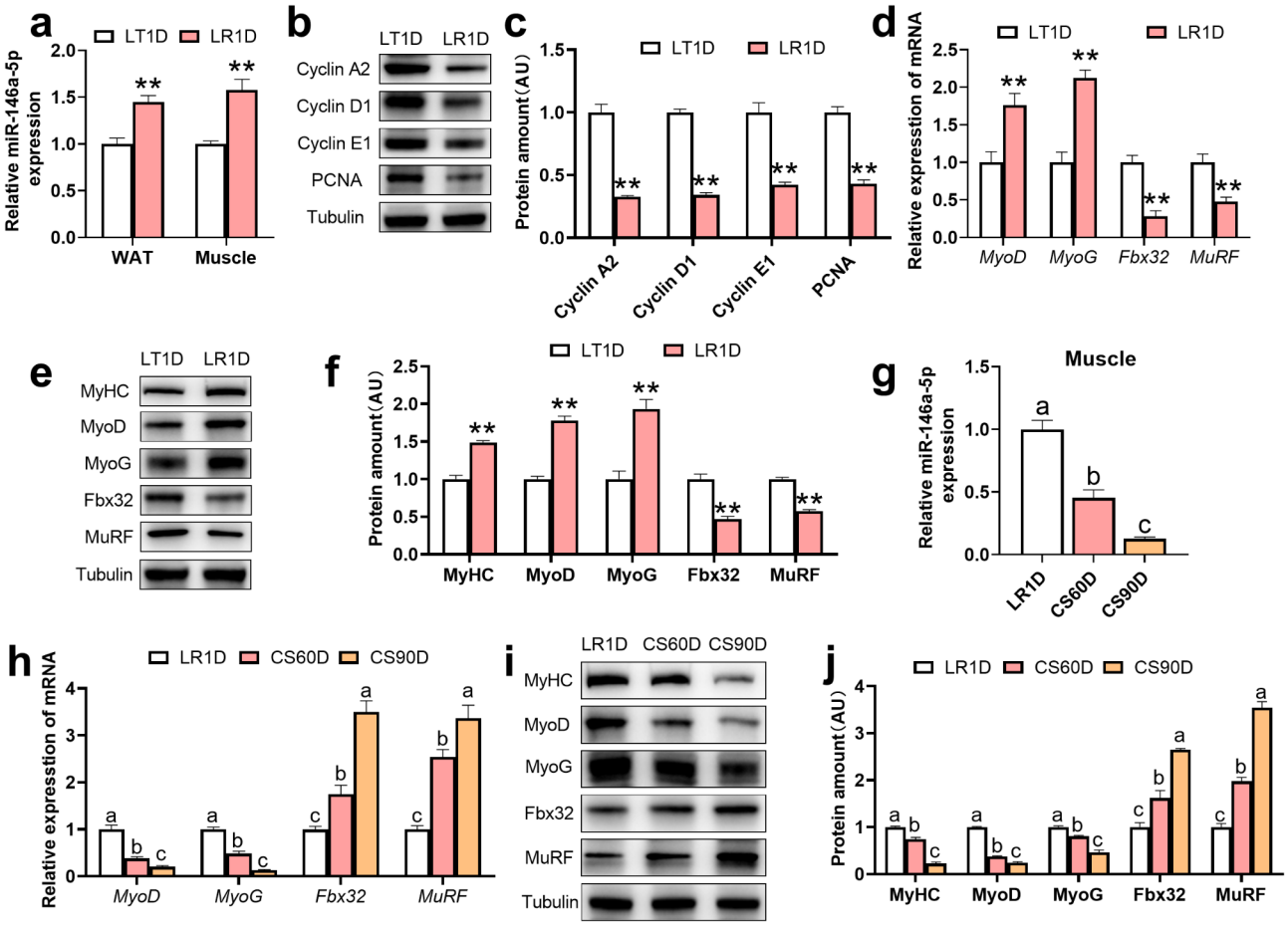

Fig. 1 Expression of miR-146a-5p in pig skeletal muscle tissues and skeletal muscle development characteristics. (**a**) The expression level of miR-146a-5p was quantified ($n=5$). (**b**, **c**) Western blotting was used to evaluate the protein abundance of proliferation-related markers, including Cyclin A2, Cyclin D1, Cyclin E1, and PCNA ($n=4$). (**d**) qPCR analysis was performed to quantify the mRNA levels of muscle differentiation markers MyoD and MyoG, along with muscle atrophy-associated genes Fbx32 and MuRF ($n=4$). (**e**, **f**) Protein expression of muscle differentiation markers MyHC, MyoD, MyoG, and muscle atrophy-related proteins Fbx32 and MuRF were measured by Western blot, followed by statistical analysis ($n=4$). (**g**) miR-146a-5p expression was measured ($n=5$). (**h**) The mRNA levels of MyoD, MyoG, Fbx32, and MuRF were assessed by qPCR ($n=5$). (**i**, **j**) Western blot analysis was conducted to detect protein levels of MyHC, MyoD, MyoG, Fbx32, and MuRF, and the results were statistically analyzed ($n=4$). Note: LT1D, 1 day after the birth of Lantang piglets; LR1D, 1 day after the birth of Landrace piglets; CS60D, 60 days after the birth of ternary hybrid pigs; CS90D, 90 days after the birth of ternary hybrid pigs. Data are presented as means ± SEM. Statistical analysis was performed using either an unpaired Student's t-test or one-way ANOVA to compare groups. A significance level of $^{*}P<0.05$ and $^{**}P<0.01$ was considered statistically significant. The letters a, b, and c represent different levels of significance between groups: distinct letters indicate a significant difference, whereas identical letters suggest no significant difference

and protein abundance of the differentiation markers MyoD and MyoG, in the skeletal muscles of aged mice. Both mRNA expression and protein levels of the skeletal muscle atrophy genes Fbx32 and MuRF increased concurrently (Fig. 2f-h). In conclusion, reduced miR-146a-5p levels in aged mice hindered skeletal muscle differentiation and worsened muscle atrophy, underscoring its critical role in muscle development and aging regulation.

Effect of miR-146a-5p on proliferation and differentiation of porcine MuSCs

This study isolated pig MuSCs to investigate the biological roles of miR-146a-5p, particularly its effects on cell proliferation and differentiation. First, the extracted MuSCs were characterized. In growth medium (GM), the early proliferative myofibroblast marker Pax7 was positive in cells up to 85%, indicating that these cells were myogenic precursor cells. When changed to differentiation medium (DM), an increase in the number of myotubes and a more pronounced fusion were observed on the 5th day, and the differentiation marker MyHC was successfully enriched in MuSCs-DM (Fig. 3a). Western Blot analysis indicated significantly elevated expression levels of Cyclin A2, Cyclin D1, Cyclin E1, and Pax7 in GM culture relative to DM (Fig. 3b). In DM, the expression of MyoG and MyoD was significantly elevated compared to GM (Fig. 3c). These outcomes confirmed the successful extraction of porcine MuSCs. We investigated the impact

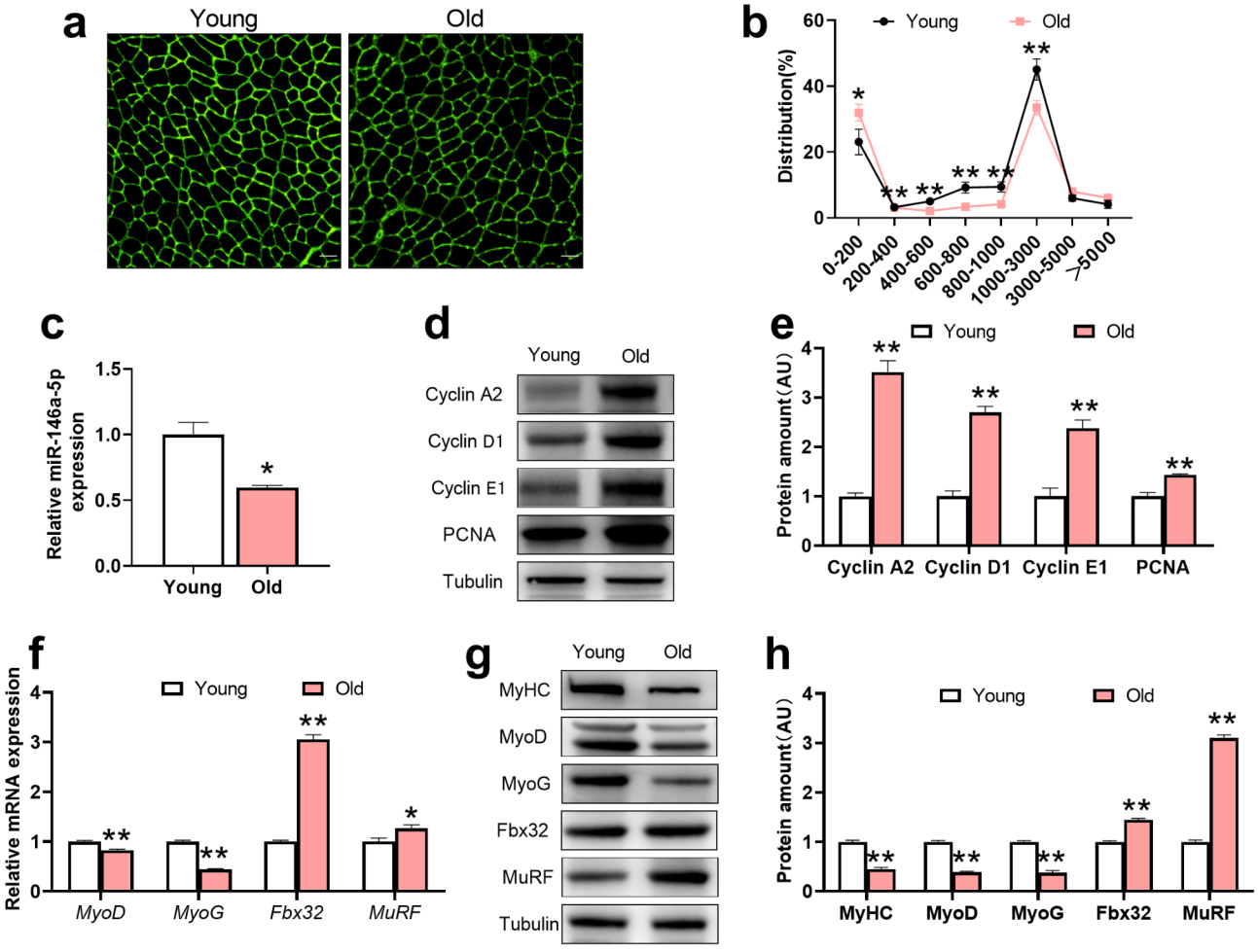

Fig. 2 Expression and developmental characteristics of miR-146a-5p in mouse skeletal muscle tissue. (**a**, **b**) TA staining was performed using Laminin (green) (scale bar = 50 μm), and muscle fiber area distribution was statistically analyzed ($n = 8$). (**c**) miR-146a-5p expression was quantified ($n = 4$). (**d**, **e**) Western blotting was performed to evaluate the protein levels of proliferation-related markers Cyclin A2, Cyclin D1, Cyclin E1, and PCNA, followed by statistical analysis ($n = 4$). (**f**) The mRNA expression of muscle differentiation markers MyoD and MyoG, and muscle atrophy markers Fbx32 and MuRF, was assessed via qPCR ($n = 4$). (**g**, **h**) Protein levels of muscle differentiation markers MyHC, MyoD, MyoG, and atrophy-related proteins Fbx32 and MuRF were determined using Western blotting, with statistical evaluation ($n = 4$). Data are expressed as means ± SEM, with significance determined by unpaired Student's t-test or one-way ANOVA between groups: $^{*}P < 0.05$, $^{**}P < 0.01$

of miR-146a-5p on MuSCs proliferation and differentiation through cell transfection using miR-146a-5p mimics and its negative control (NC), as well as miR-146a-5p inhibitors and its inhibitor negative control (INC) (Fig. 3d and k). The use of miR-146a-5p mimics significantly reduced both the number of EdU-positive cells and cell viability, as shown by EdU staining and CCK-8 assays, with these effects being counteracted by the miR-146a-5p inhibitor (Fig. 3e-g). miR-146a-5p mimics significantly reduced the protein levels of PCNA and both mRNA and protein expression of Cyclin D1, Cyclin A2, and Cyclin E1, while miR-146a-5p suppression produced the opposite effect (Fig. 3h-j). miR-146a-5p mimics enhanced MyoG and MyoD mRNA expression and reduced Fbx32 and MuRF mRNA levels in MuSCs. Conversely, the miR-146a-5p inhibitor produced opposite effects (Fig. 3l). Western blot analysis revealed that miR-146a-5p mimics increased MyHC protein levels in MuSCs, while the miR-146a-5p inhibitor markedly decreased MyHC expression (Fig. 3m-n). Overall, miR-146a-5p is crucial in controlling the growth and differentiation of MuSCs and might influence their biological activities by modulating cell cycle proteins and skeletal muscle differentiation markers.

Effects of adipose-specific miR-146a-5p knockdown on skeletal muscle differentiation, mitochondrial autophagy, and apoptosis in mice

The study utilized CRISPR-Cas9 to create an adipose-specific miR-146a-5p knockout mouse model (aKO mice, $Cre^{+/-}Loxp^{+/+}$) to examine the effects of miR-146a-5p deletion in adipose tissue on skeletal muscle development, using Flox mice ($Loxp^{+/+}$) as controls (Fig. 4a).

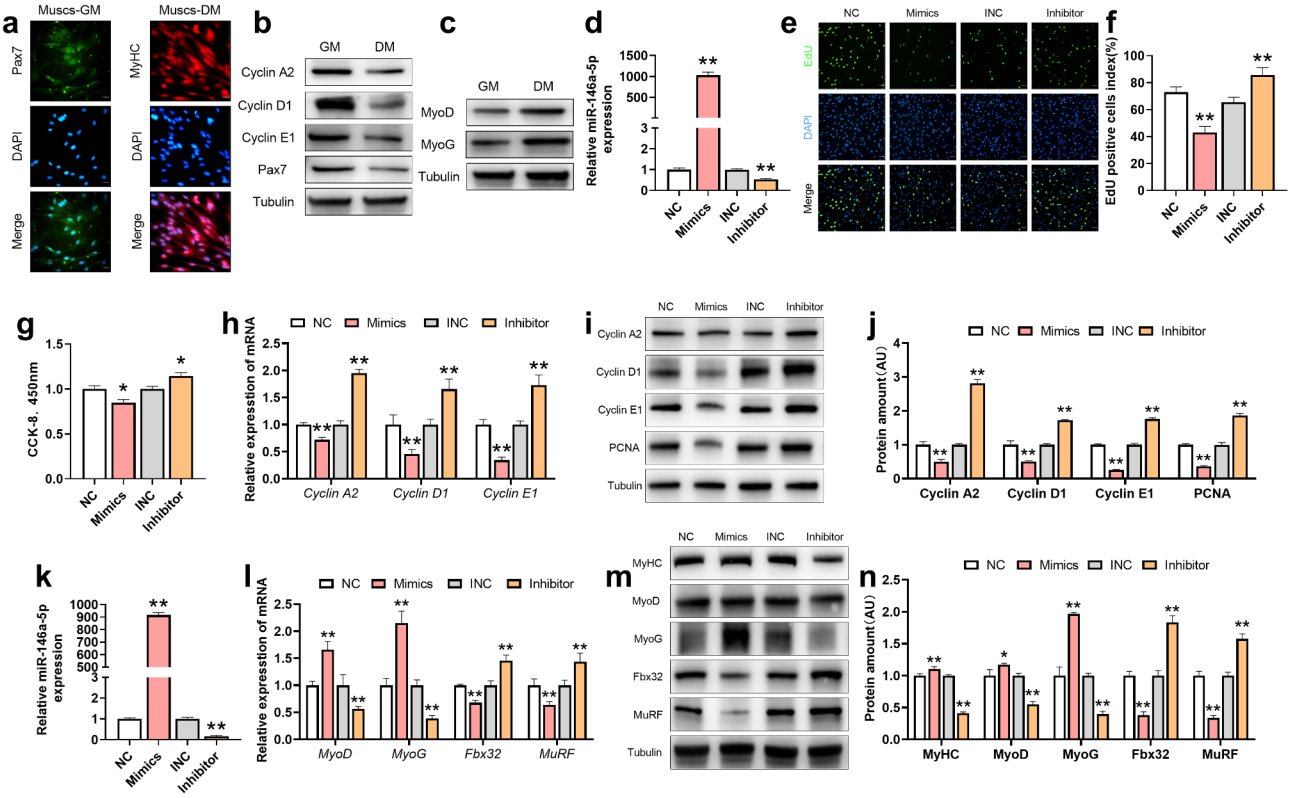

Fig. 3 Effect of miR-146a-5p on proliferation and differentiation of porcine skeletal muscle satellite cells. (**a**) Immunofluorescence staining was performed to visualize GM, a proliferation marker (Pax7), and DM, a differentiation marker (MyHC), followed by analysis under a fluorescence microscope ($n=4$). (**b**) Protein expression levels of Cyclin A2, Cyclin D1, Cyclin E1, and Pax7 were evaluated using Western blot ($n=4$). (c**c**) The expression of MyoD and MyoG proteins was assessed by Western blotting ($n=4$). (**d**) The relative expression of miR-146a-5p was measured ($n=6$). (**e**, **f**) Immunofluorescence results and statistical analysis of the EdU proliferation assay were performed ($n=6$). (**g**) CCK8 assay results were obtained. (**h**) mRNA levels of Cyclin A2, Cyclin D1, and Cyclin E1 were quantified by qPCR ($n=4$). (**i**, **j**) Western blotting was used to analyze the protein expression of proliferation markers Cyclin A2, Cyclin D1, Cyclin E1, and PCNA, followed by statistical evaluation ($n=4$). (**k**) miR-146a-5p expression was quantified ($n=6$). (**l**) The mRNA expression of muscle differentiation markers MyoD and MyoG, along with muscle atrophy genes Fbx32 and MuRF, was measured by qPCR ($n=6$). (**m**, **n**) Western blot analysis and statistical evaluation of protein levels of muscle differentiation markers MyHC, MyoD, MyoG, and atrophy-related genes Fbx32 and MuRF were conducted ($n=4$). Data are expressed as means ± SEM, with significance determined by unpaired Student's t-test or one-way ANOVA between groups: $^{*}P<0.05$, $^{**}P<0.01$

Both genotype identification (Fig. 4a) and real-time fluorescence quantitative PCR (Fig. 4b) analyses confirmed a significant reduction in miR-146a-5p expression in the WAT of aKO mice compared to Flox mice, validating the successful establishment of the aKO mouse model. In aKO mice, the TA muscle showed a marked reduction in miR-146a-5p expression. This research evaluated the impact of deleting adipose-specific miR-146a-5p on muscle development by comparing skeletal muscle growth in young and aged 146aKO mice. Histological analysis of TA muscles showed more pronounced muscle wasting in older 146aKO mice compared to their younger counterparts. The study observed an increase in smaller muscle fibers (0–200 μm²) and a decrease in larger fibers (1000–5000 μm²) (Figure S1a-b). RT-qPCR analysis revealed that miR-146a-5p levels were significantly lower in the TA muscle of aged 146aKO mice compared to their younger counterparts (Figure S1c). RT-qPCR and Western Blot analyses confirmed elevated levels of proliferation-related proteins in the skeletal muscle of aged 146aKO mice (Figure S1d-e). In aged 146aKO mice, mRNA and protein levels of atrophy-related genes Fbx32 and MuRF were significantly elevated, whereas differentiation-related gene expression was notably reduced compared to younger mice (Figure S1f-h). These findings are similar to those characterizing skeletal muscle development in wild-type mice at different ages, further confirming that adipose-specific miR-146a-5p deletion has an age-dependent effect on skeletal muscle development.

MuSCs are vital for the maintenance and regeneration of skeletal muscle. MuSCs were isolated from the muscle tissues of Flox and aKO mice to evaluate the impact of adipose-specific miR-146a-5p deletion on their proliferation and differentiation. The study demonstrated a notable decrease in miR-146a-5p expression in MuSCs derived from aKO mice (aKO-MuSCs) (Fig. 4c).

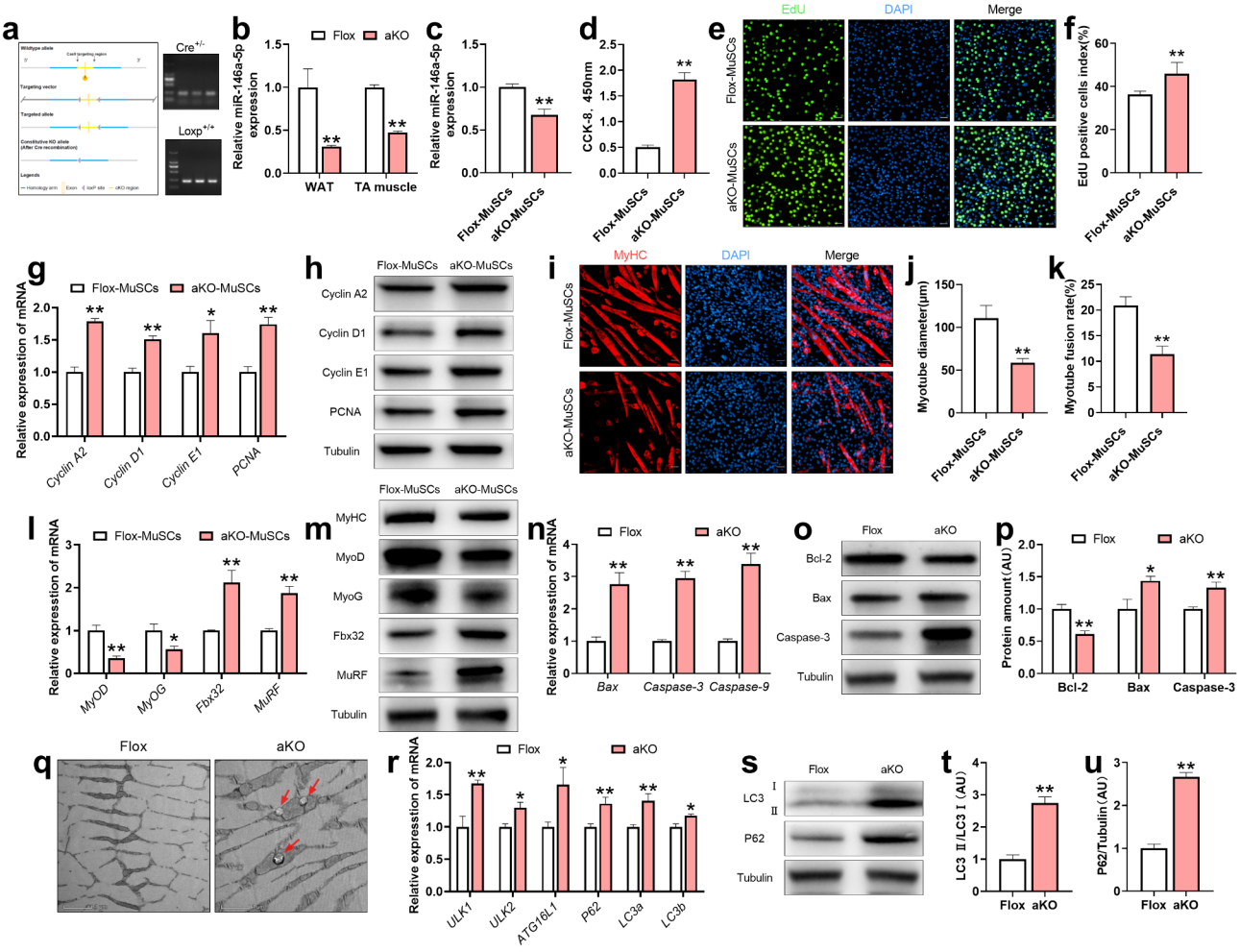

Fig. 4 Effects of adipose-specific miR-146a-5p knockdown on skeletal muscle differentiation, mitochondrial autophagy, and apoptosis in mice. (**a**) Schematic overview and genotypic characterization of aKO mice. (**b**) miR-146a-5p expression was measured in the WAT and TA muscles of Flox and aKO mice ($n=6$). (**c**) The relative expression of miR-146a-5p in Flox-MuSCs and aKO-MuSCs was quantified ($n=6$). (**d**) CCK-8 assay results for Flox-MuSCs and aKO-MuSCs were obtained ($n=4$). (**e**, **f**) EdU staining images and corresponding statistical analysis for Flox-MuSCs and aKO-MuSCs (scale bar = 50 μm) ($n=5$). (**g**) RT-qPCR analysis of Cyclin A2, Cyclin D1, Cyclin E1, and PCNA expression in Flox-MuSCs and aKO-MuSCs ($n=4$). (**h**) Protein levels of Cyclin A2, Cyclin D1, Cyclin E1, and PCNA were determined by Western blot in Flox-MuSCs and aKO-MuSCs ($n=4$). (**i**-**k**) Immunofluorescence images of MyHC-stained muscle fibers in Flox-MuSCs and aKO-MuSCs ($n=6$) (scale bar = 50 μm). (**l**) mRNA expression of muscle differentiation markers MyoD and MyoG, as well as atrophy-related genes Fbx32 and MuRF, was assessed by qPCR in Flox-MuSCs and aKO-MuSCs ($n=6$). (**m**) Protein expression of MyHC, MyoD, MyoG, Fbx32, and MuRF was analyzed by Western blot in Flox-MuSCs and aKO-MuSCs ($n=6$). (**n**) The relative mRNA expression of Bax, Caspase-3, and Caspase-9 in TA muscles of Flox and aKO mice was quantified. (**o**, **p**) Western blot analysis of Bcl-2, Bax, and Caspase-3 protein levels in TA muscles of Flox and aKO mice. (**q**) Electron microscopy of mitochondrial autophagy in TA muscle from Flox and aKO mice, with red arrows indicating autophagic vacuoles (scale bar = 1 μm). (**r**) RT-qPCR analysis of ULK1, ULK2, ATG16L1, P62, LC3a, and LC3b expression in TA muscles of Flox and aKO mice ($n=6$). (**s**-**u**) Western blot analysis of LC3 and P62 protein expression in TA muscles of Flox and aKO mice, with statistical analysis ($n=4$). Data are expressed as means ± SEM, with significance determined by unpaired Student's t-test or one-way ANOVA between groups: $^{*}P<0.05$, $^{**}P<0.01$

Additionally, adipose-specific deletion of miR-146a-5p led to a notable increase in cell viability and EdU-positive rates in aKO-MuSCs (Fig. 4e-f). Furthermore, the mRNA levels of PCNA, Cyclin D1, Cyclin A2, and Cyclin E1 were markedly elevated in aKO-MuSCs (Fig. 4g), with Western Blot confirming a similar trend at the protein level (Fig. 4h, Figure S2a). Myotube diameter and nuclear fusion index were significantly lower in aKO-MuSCs (Fig. 4i-k). The expression levels of MyoD and MyoG, both at the mRNA and protein levels, along with MyHC protein, were significantly reduced. The mRNA and protein levels of the atrophy-related genes Fbx32 and MuRF significantly increased (Fig. 4l-m, Figure S2b). These findings suggest that adipose-specific miR-146a-5p knockdown exacerbates MuSCs atrophy in mice. This study investigated apoptosis and autophagy in the skeletal muscle of aKO mice, given the association between miR-146a-5p deletion and MuSCs atrophy, as well as the established links between skeletal muscle atrophy, apoptosis, and autophagy. RT-qPCR analysis indicated a

marked increase in the expression of pro-apoptotic genes Bax, Caspase-3, and Caspase-9 in the TA muscle of aKO mice (Fig. 4n).

Immunoblotting revealed a significant decrease in Bcl-2 protein levels, accompanied by increased Bax and Caspase-3 levels in the TA muscles of aKO mice (Fig. 4o-p). Electron microscopy analysis showed swelling and autophagic vacuoles in mitochondria in TA muscles of aKO mice (Fig. 4q). RT-qPCR analysis demonstrated a notable elevation in mRNA levels of autophagy-related genes ULK1, ULK2, ATG16L1, P62, LC3a, and LC3b in the TA muscles of aKO mice relative to controls (Fig. 4r). Western blot analysis further confirmed the increased expression of autophagy-related proteins LC3 and P62 in the TA muscles of aKO mice (Fig. 4s-u). Experiments demonstrated that aKO-MuSCs exhibited a significant decrease in Bcl-2 mRNA and protein levels, while Bax and Caspase-3 levels were notably elevated, accompanied by an upregulation of Caspase-9 mRNA (Figure S2c-e). RT-qPCR and Western blot analyses similarly indicated that autophagy-related genes and proteins were significantly upregulated in aKO-MuSCs, reflecting the changes observed in the skeletal muscle tissues of aKO mice (Figure S2f-i). In summary, the adipose-specific miR-146a-5p deletion in the mouse model enhanced MuSCs proliferation while simultaneously hindering skeletal muscle differentiation and worsening muscle atrophy. These changes, possibly through apoptosis and autophagy pathways, underscore miR-146a-5p's crucial role in muscle development and provide a new understanding of the molecular mechanisms behind skeletal muscle atrophy.

Effect of miR-146a-5p on apoptosis, autophagy, ROS, and ATP during C2C12 cell differentiation

We examined the impact of miR-146a-5p on apoptosis, autophagy, ROS, and ATP levels in C2C12 cells by transfecting them with miR-146a-5p mimics or inhibitors and conducting various experiments (Fig. 5a). Flow cytometry analysis revealed that miR-146a-5p mimics significantly decreased apoptosis, whereas the inhibitor enhanced it (Fig. 5b-c). RT-qPCR analysis demonstrated that mimics increased Bcl-2 expression while decreasing Bax, Caspase-3, and Caspase-9 levels, with these effects being reversed by the inhibitor (Fig. 5d). Western blot analysis confirmed miR-146a-5p's regulatory influence on apoptosis-related proteins (Fig. 5e-f). Regarding autophagy, RT-qPCR showed that the miR-146a-5p mimics markedly reduced the mRNA levels of autophagy-related genes (ULK1, ULK2, ATG16L1, P62, LC3a, and LC3b), whereas the inhibitor significantly elevated their expression (Fig. 5g). Immunoblotting revealed that miR-146a-5p mimics notably decreased LC3 and P62 protein levels, while the inhibitor markedly elevated their expression (Fig. 5h-j). Moreover, ROS are crucial in the atrophy and aging of skeletal muscle and help maintain mitochondrial balance by encouraging mitochondrial autophagy. Our experiments demonstrated that elevated miR-146a-5p expression significantly reduced ROS production and increased ATP levels in C2C12 cells. Conversely, miR-146a-5p inhibitor enhanced ROS generation and reduced ATP levels (Fig. 5k-m). miR-146a-5p appears to significantly influence cell differentiation in C2C12 cells by inhibiting apoptosis, autophagy, and ROS production, although reduced ATP levels might activate autophagy.

Overexpression of miR-146a-5p in Wat adipose tissue sEV alleviates myofiber atrophy, apoptosis, and autophagy

sEV are crucial for intercellular communication, transporting biomolecules like lipids, proteins, and miRNAs to target cells. This study aimed to explore whether adipocytes influence myofiber development via sEV containing miR-146a-5p. First, we extracted WAT-derived sEV (WAT-sEV) from Flox mice and aKO mice, observed their morphology using transmission electron microscopy (Fig. 6a), and determined that their diameters were mainly distributed between 20 and 170 nm by nanometer particle size analyzer (Fig. 6b). Furthermore, Western blot analysis confirmed the presence of typical sEV markers Alix, TSG101, CD63, and CD9 in WAT-sEV, while the endoplasmic reticulum marker calnexin was not detected (Fig. 6c), validating the successful isolation of WAT-sEV. qPCR analysis indicated a notable decrease in miR-146a-5p levels in sEV derived from adipose tissue of aKO mice relative to Flox mice (Fig. 6d). To further verify the biological function of WAT-sEV, we treated C2C12 cells with PKH67 fluorescent labeling and observed their intracellular uptake after 12 h. Immunofluorescence staining results showed that sEV successfully entered the cytoplasm (Fig. 6e). In subsequent cell culture experiments, co-transfection of C2C12 cells with sEV from Flox mice (Flox-sEV) or aKO mice (aKO-sEV) alongside miR-146a-5p mimics (aKO-sEV + M) led to a notable increase in myofiber diameter and nuclear fusion percentage. C2C12 cells co-transfected with either aKO-sEV or Flox-sEV alongside the miR-146a-5p inhibitor (Flox-sEV + I) exhibited a significant reduction in both myofiber diameter and nuclear fusion ratio (Fig. 6f-g, Figure S3). Western Blot analysis revealed that treatments with Flox-sEV and aKO-sEV + M significantly elevated the expression of muscle-specific markers MyHC and MyoD while reducing the levels of atrophy-related proteins Fbx32 and MuRF. Conversely, aKO-sEV and Flox-sEV + I treatments showed the opposite effect, significantly reducing MyHC and MyoD levels while elevating Fbx32 and MuRF (Fig. 6g-i). Western blot analysis demonstrated that Flox-sEV and aKO-sEV + M increased Bcl-2 expression while decreasing Caspase-3 and Bax levels. Conversely,

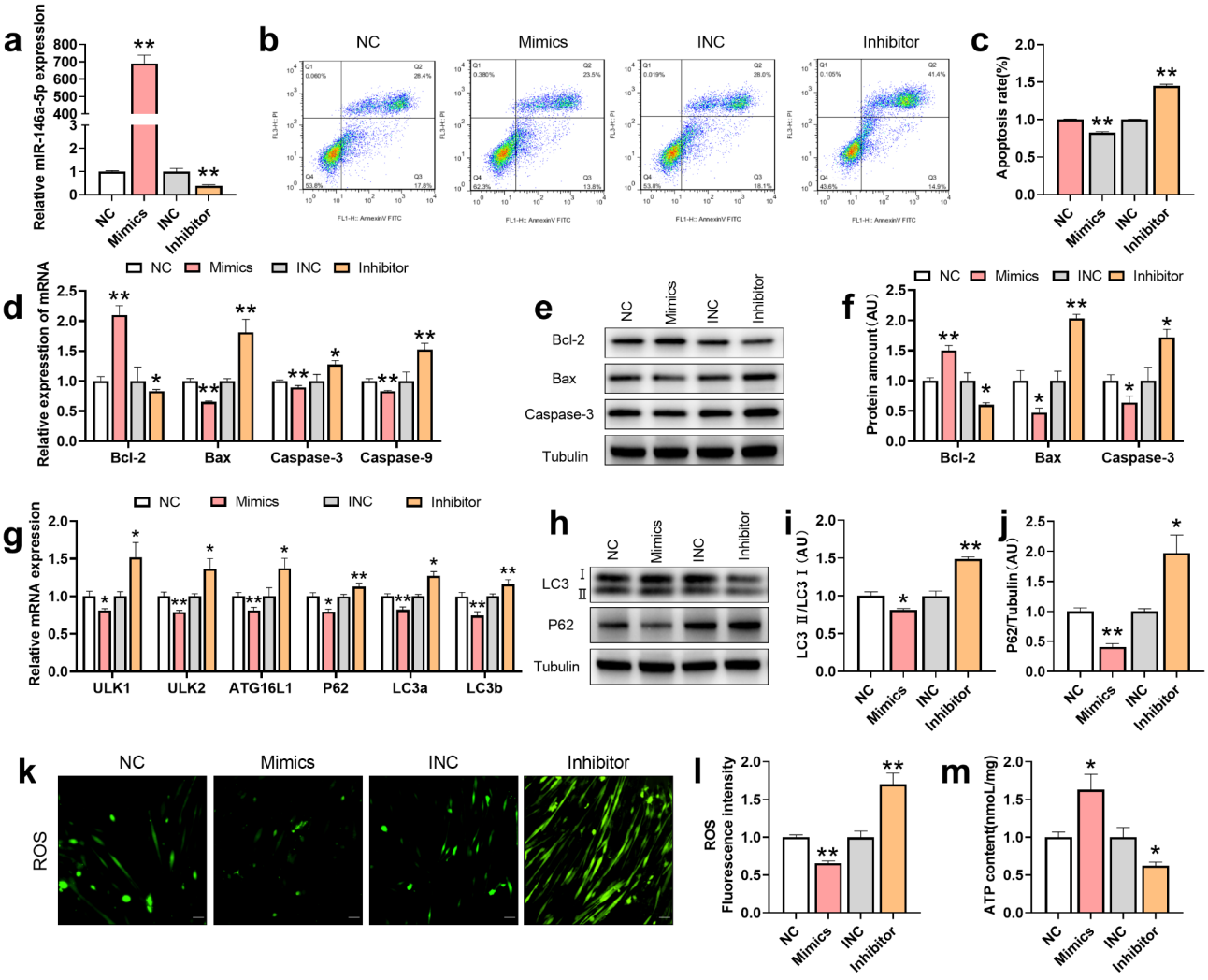

Fig. 5 Effect of miR-146a-5p on apoptosis, autophagy, ROS, and ATP during C2C12 cell differentiation. (**a**) Expression of miR-146a-5p was measured in C2C12 cells following transfection with mimics and inhibitors ($n=6$). (**b**, **c**) Flow cytometry analysis was performed to determine the apoptotic rate ($n=4$). (**d**) mRNA levels of Bcl-2, Bax, Caspase-3, and Caspase-9 in C2C12 cells were quantified ($n=9$). (**e**, **f**) Protein expression of Bcl-2, Bax, and Caspase-3 was assessed by Western blot, followed by statistical analysis ($n=4$). (**g**) RT-qPCR analysis was conducted to evaluate the expression of ULK1, ULK2, ATG16L1, P62, LC3a, and LC3b mRNA in C2C12 cells ($n=9$). (**h-j**) Western blotting was used to determine protein levels of LC3 and P62, with statistical analysis of the results ($n=4$). (**k**, **l**) ROS levels were quantified through fluorescence microscopy (green fluorescence) with representative images and a scale bar of 50 μm ($n=6$). (**m**) Intracellular ATP levels were measured to assess cellular energy status ($n=4$). Data are expressed as means ± SEM, with significance determined by unpaired Student's t-test or one-way ANOVA between groups: $^{*}P<0.05$, $^{**}P<0.01$

aKO-sEV and Flox-sEV + I counteracted these effects by decreasing Bcl-2 levels and increasing Bax and Caspase-3 levels (Fig. 6j-k). The analysis of autophagy revealed that Flox-sEV and aKO-sEV + M significantly reduced the expression of LC3 and P62 autophagy markers, while aKO-sEV and Flox-sEV + I enhanced their expression (Fig. 6l-m). Our findings indicate that overexpressing miR-146a-5p counteracts aKO-sEV-induced inhibition of myofiber differentiation, atrophy, apoptosis, and autophagy while enhancing C2C12 cell differentiation. This research highlights miR-146a-5p's crucial role in myofiber development through WAT-sEV, suggesting a potential therapeutic approach for skeletal muscle dystrophies.

MiR-146a-5p regulates skeletal muscle differentiation, regenerative repair, mitochondrial autophagy, and apoptosis through WAT-sEV in mice

To further validate the role of WAT-sEV and its contained miR-146a-5p in regulating skeletal muscle differentiation, atrophy, repair and regeneration, mitochondrial autophagy, and apoptosis in mice. In this study, wild-type aged mice were selected as experimental subjects. Initially, PKH67 was employed to fluorescently label WAT-sEV. Labeled WAT-sEV was administered into the TA muscle of mice. The findings indicated that these particles were primarily localized in the gastrocnemius (GAS) and TA muscles. Once in the systemic circulation, they

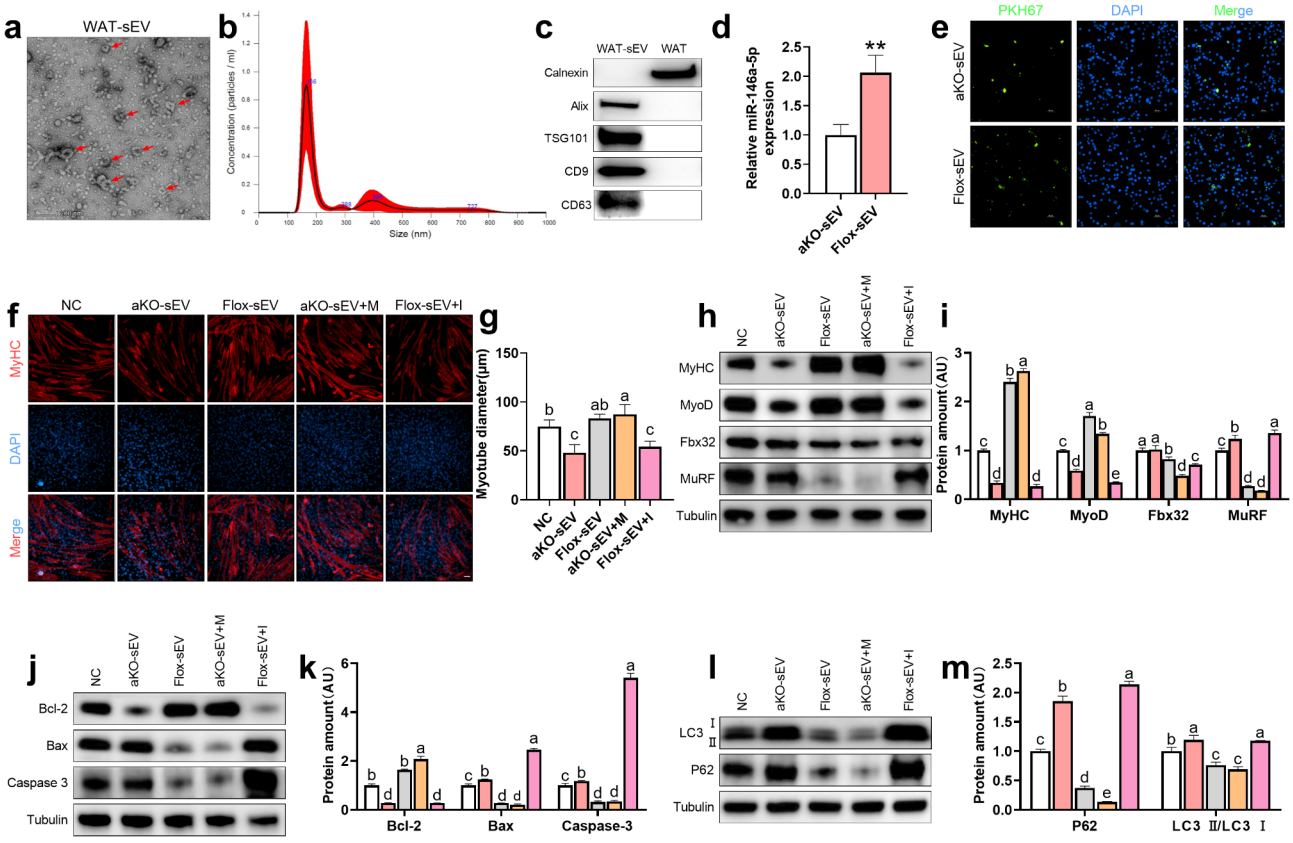

Fig. 6 Overexpression of miR-146a-5p in wat adipose tissue small extracellular vesicles alleviates myofiber atrophy, apoptosis, and autophagy. (**a**) Electron microscopy results of WAT-sEV in vitro (scale bar = 200 nm). (**b**) Size distribution of WAT-sEV. (**c**) Expression of marker proteins Alix, TSG101, CD9, and CD63 in WAT-derived sEVs, and Calnexin, a marker for the endoplasmic reticulum, in WAT ($n = 4$). (**d**) miR-146a-5p expression was quantified by quantitative PCR in four types of WAT-sEVs (Flox-sEV and aKO-sEV) ($n = 4$). (**e**) Fluorescence images were captured of C2C12 cells treated with PKH67-labeled sEVs ($n = 4$). (**f**) Immunofluorescence staining of C2C12 cells induced to differentiate and mature after treatment with aKO-sEV, Flox-sEV, or co-incubation with mimics or inhibitors. MyHC signals denote the myofibril phenotype, while DAPI staining identifies the nucleus (scale bar = 50 μm) ($n = 6$). (**g**) MyHC myofiber area was quantified. (**h**, **i**) Western blot analysis and statistical evaluation of MyHC, MyoD, Fbx32, and MuRF protein levels following treatment of C2C12 cells with aKO-sEV, Flox-sEV, or co-incubation with mimics and inhibitors ($n = 4$). (**j**, **k**) Western blot analysis and statistical evaluation of Bcl-2, Bax, and Caspase-3 protein levels in C2C12 cells treated with aKO-sEV or Flox-sEV, with or without mimics and inhibitors ($n = 4$). (**l**, **m**) Statistical results of P62 and LC3 protein expression after C2C12 cells were treated with aKO-sEV, Flox-sEV, or co-incubated with mimics and inhibitors ($n = 4$). Data are presented as means ± SEM. Statistical analysis was performed using either an unpaired Student's t-test or one-way ANOVA to compare groups. A significance level of $^{*}P < 0.05$ and $^{**}P < 0.01$ was considered statistically significant. The letters a, b, and c represent different levels of significance between groups: distinct letters indicate a significant difference, whereas identical letters suggest no significant difference

accumulated in epididymal WAT and inguinal WAT, as well as intestinal fat (Fig. 7a-b). PBS, Flox-sEV, and aKO-sEV were continuously injected into the TA muscle over a 17-day cycle, with muscle samples collected on day 19 for analysis (Fig. 7c). The study found significantly higher miR-146a-5p levels in the TA muscle of aged mice treated with Flox-sEV compared to the aKO-sEV group (Fig. 7d). Concurrently, the expression of differentiation-related genes was markedly upregulated, while proliferation and atrophy-related genes were significantly downregulated (Fig. 7e-f, Figure S4a-d). In addition, the changes in myofiber morphology further supported this result, as the area of myofibers (> 5000 μm²) in TA muscles of aged mice was significantly increased and smaller myofibers (< 200 μm²) were significantly decreased after Flox-sEV injection, compared with the aKO-sEV group (Fig. 7g-h). Further analysis revealed a significant rise in MyoD and Pax7 fluorescence intensity in the TA muscle of Flox-sEV-injected mice, indicating enhanced skeletal muscle repair and regeneration (Fig. 7i-l). Additionally, apoptosis markers were notably reduced in the TA muscles of aged mice treated with Flox-sEV (Fig. 7m-n). Importantly, autophagy was significantly improved in the TA muscles of aged mice receiving Flox-sEV, while mitochondrial autophagy was observed in the aKO-sEV group (Fig. 7o-q, Figure S4e-f). These findings underscore the essential function of miR-146a-5p, abundant in Flox-sEV, in facilitating skeletal muscle recovery by promoting differentiation, repair, and regeneration, as well as inhibiting muscle

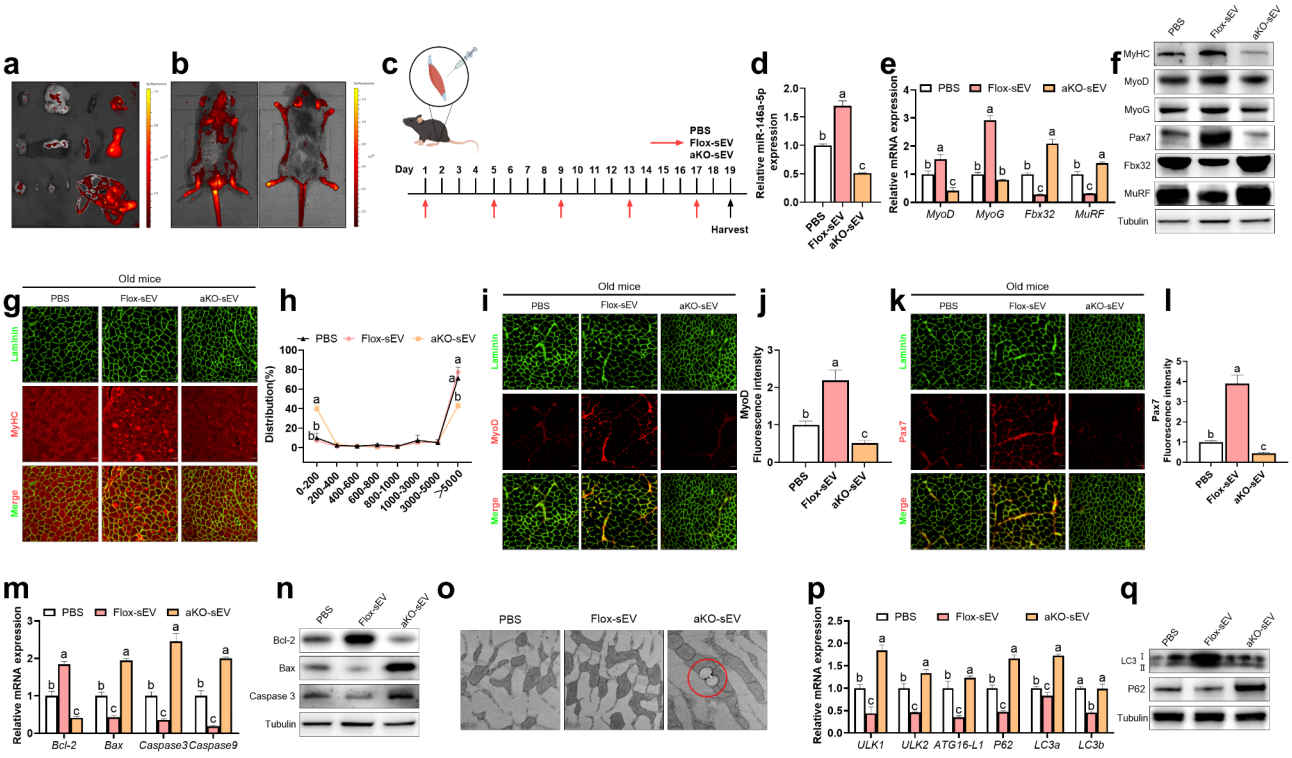

Fig. 7 MiR-146a-5p regulates skeletal muscle differentiation, regenerative repair, mitochondrial autophagy, and apoptosis through WAT-sEV in mice. (**a**) In vivo imaging of PKH67-labeled WAT-sEVs 12 h after injection into the TA muscle of aged mice. (**b**) Imaging of various organs following injection of PKH67-labeled WAT-sEVs into the TA muscle of aged mice for 12 h. The isolated organs (from left to right) include the heart, liver, spleen, lungs, kidneys, brown fat, iWAT, eWAT, GAS muscle, soleus muscle, TA muscle, extensor digitorum longus muscle, and intestinal fat. (**c**) Schematic representation of TA muscle injections of PBS, Flox-sEV, and aKO-sEV in 18-month-old aged mice. (**d**) miR-146a-5p expression in the TA muscle of aged mice 12 h after receiving PBS, Flox-sEV, or aKO-sEV ($n=6$). (**e**) mRNA expression levels of skeletal muscle differentiation genes MyoD and MyoG, and atrophy-related genes Fbx32 and MuRF in the TA muscle after injection of PBS, Flox-sEV, or aKO-sEV ($n=6$). (**f**) Western blot analysis of protein expression for skeletal muscle differentiation and atrophy markers in the TA muscle following PBS, Flox-sEV, or aKO-sEV injections ($n=4$). (**g**, **h**) Representative plots of MyHC staining cross-sectional areas and statistical analysis in the TA muscle after PBS, Flox-sEV, or aKO-sEV treatment (scale bar = 50 μm) ($n=6$). (**i**, **j**) Quantification and statistical analysis of MyoD staining and immunofluorescence in the TA muscle after injections of PBS, Flox-sEV, or aKO-sEV (scale bar = 50 μm) ($n=6$). (**k**, **l**) Statistical analysis of Pax7 staining and immunofluorescence in the TA muscle after injection of PBS, Flox-sEV, or aKO-sEV (scale bar = 50 μm) ($n=6$). (**m**) Quantitative PCR analysis of Bcl-2, Bax, Caspase-3, and Caspase-9 mRNA expression in the TA muscle after PBS, Flox-sEV, or aKO-sEV injection ($n=6$). (**n**) Western blot assessment of Bcl-2, Bax, and Caspase-3 protein expression in the TA muscle of aged mice after treatment with PBS, Flox-sEV, or aKO-sEV ($n=4$). (**o**) Electron microscopy of mitochondrial autophagy in the TA muscle after PBS, Flox-sEV, or aKO-sEV injections, with autophagic vacuoles indicated by red circles (scale bar = 500 nm). (**p**) RT-qPCR analysis of ULK1, ULK2, ATG16L1, P62, LC3a, and LC3b mRNA expression in the TA muscle following PBS, Flox-sEV, or aKO-sEV injection ($n=6$). (**q**) Protein levels of LC3 and P62 in the TA muscle after injection of PBS, Flox-sEV, or aKO-sEV, determined by Western blot ($n=4$). Data are presented as means ± SEM. Statistical analysis was performed using either an unpaired Student's t-test or one-way ANOVA to compare groups. A significance level of $^{*}P<0.05$ and $^{**}P<0.01$ was considered statistically significant. The letters a, b, and c represent different levels of significance between groups: distinct letters indicate a significant difference, whereas identical letters suggest no significant difference

atrophy and modulating apoptosis and mitochondrial autophagy.

MiR-146a-5p regulates skeletal muscle cell differentiation, mitochondrial autophagy, and apoptosis by targeting Fbx32

Transcriptomic and bioinformatics analyses indicate that miR-146a-5p potentially affects mitochondrial autophagy in skeletal muscle through its interaction with Fbx32 (Fig. 8a). To directly assess this interaction, we performed mutational analysis of the miR-146a-5p binding site on Fbx32 mRNA. Fbx32 wild-type (pmirGLO-WT), mutation (pmirGLO-MUT), and deletion (pmirGLO-DEL) constructs were co-transfected with either a negative control (NC) or miR-146a-5p mimics in 293T cells. The co-transfection of miR-146a-5p mimics with pmirGLO-WT significantly reduced dual luciferase activity, confirming the interaction between miR-146a-5p and Fbx32. In contrast, the pmirGLO-Mutation and pmirGLO-Deletion constructs showed no change in luciferase activity, demonstrating that the mutation or deletion of the miR-146a-5p binding site abrogates the regulatory effect of miR-146a-5p on Fbx32 expression (Fig. 8b). These results provide direct evidence of the miR-146a-5p binding site's critical role in regulating Fbx32 expression through post-transcriptional mechanisms. Next, three siRNAs for

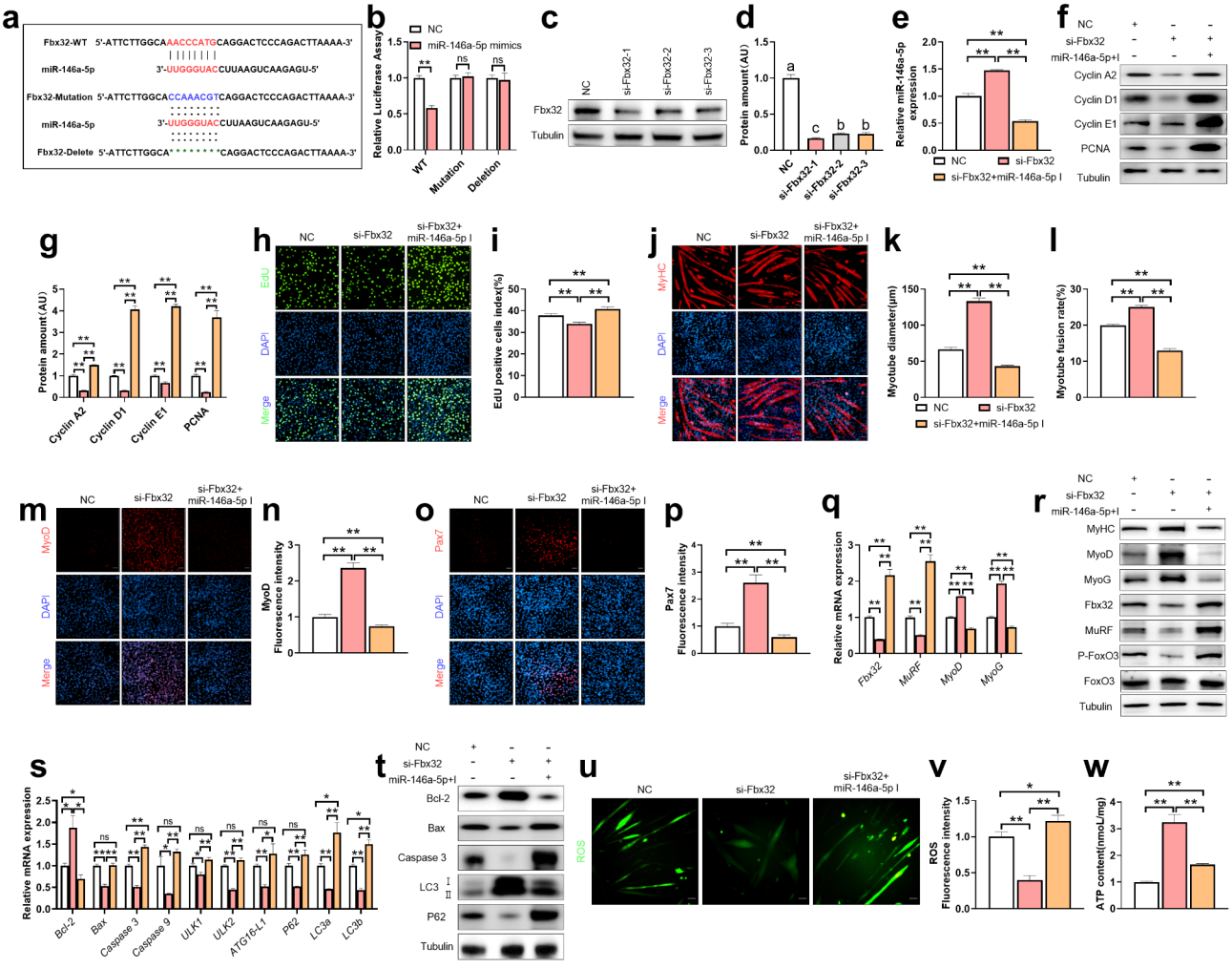

Fig. 8 MiR-146a-5p regulates skeletal muscle cell differentiation, mitochondrial autophagy, and apoptosis by targeting Fbx32. (**a**) Diagram depicting the binding sites of miR-146a-5p on Fbx32. (**b**) Results of a double luciferase assay showing fluorescence values for miR-146a-5p and Fbx32 interaction. (**c-d**) Immunoblotting and analysis of Fbx32 protein levels in C2C12 cells transfected with Fbx32 siRNA for 48 h ($n=6$). (**e**) RT-qPCR assessment of relative miR-146a-5p expression in C2C12 cells transfected with si-Fbx32 and si-Fbx32 + miR-146a-5p inhibitor ($n=6$). (**f**, **g**) Western blot analysis of proliferation-related proteins Cyclin A2, Cyclin D1, Cyclin E1, and PCNA in C2C12 cells treated with si-Fbx32 or si-Fbx32 + miR-146a-5p inhibitor ($n=4$). (**h**, **i**) EdU proliferation assay images and statistical analysis in C2C12 cells transfected with si-Fbx32 or si-Fbx32 + miR-146a-5p inhibitor ($n=6$). (**j-l**) Immunofluorescence staining for MyHC in C2C12 cells transfected with si-Fbx32 or si-Fbx32 + miR-146a-5p inhibitor, including quantification of myotube diameter and nucleus fusion (scale bar = 50 μm) ($n=6$). (**m**, **n**) Immunofluorescence analysis of MyoD (red) and DAPI (blue) after transfection with si-Fbx32 or si-Fbx32 + miR-146a-5p inhibitor (scale bar = 50 μm) ($n=6$). (**o**, **p**) Immunofluorescence staining and statistical analysis of Pax7 (red) and DAPI (blue) in C2C12 cells transfected with si-Fbx32 or si-Fbx32 + miR-146a-5p inhibitor (scale bar = 50 μm) ($n=6$). (**q**) Quantitative PCR analysis of Fbx32, MuRF, MyoD, and MyoG expression after treatment with si-Fbx32 or si-Fbx32 + miR-146a-5p inhibitor ($n=6$). (**r**) Western blot assessment of MyHC, MyoD, MyoG, Fbx32, MuRF, and p-FoxO3/FoxO3 protein expression in C2C12 cells following si-Fbx32 or si-Fbx32 + miR-146a-5p inhibitor transfection ($n=4$). (**s**) mRNA expression levels of Bcl-2, Bax, Caspase-3, Caspase-9, ULK1, ULK2, ATG16L1, P62, LC3a, and LC3b measured by RT-qPCR in C2C12 cells transfected with si-Fbx32 or si-Fbx32 + miR-146a-5p inhibitor ($n=6$). (**t**) Western blot detection of Bcl-2, Bax, Caspase-3, LC3, and P62 protein expression in C2C12 cells after transfection with si-Fbx32 or si-Fbx32 + miR-146a-5p inhibitor ($n=4$). (**u**, **v**) Representative images and quantification of ROS levels in C2C12 cells transfected with si-Fbx32 or si-Fbx32 + miR-146a-5p inhibitor using fluorescence microscopy (green fluorescence, scale bar = 50 μm) ($n=6$). (**w**) Measurement of relative intracellular ATP levels in C2C12 cells transfected with si-Fbx32 or si-Fbx32 + miR-146a-5p inhibitor ($n=4$).Data are expressed as means ± SEM, with significance determined by unpaired Student's t-test or one-way ANOVA between groups: $^{*}P<0.05$, $^{**}P<0.01$

Fbx32 were constructed in this study and verified by protein knockdown efficiency, and siFbx32-1 was selected for subsequent experiments (Fig. 8c-d). The experiment comprised three groups: NC, si-Fbx32, and si-Fbx32 with a miR-146a-5p inhibitor (si-Fbx32 + miR-146a-5p I). In C2C12 cells, si-Fbx32 transfection significantly increased miR-146a-5p levels, while a si-Fbx32 + miR-146a-5p I notably reduced its expression (Fig. 8e). Western blot analysis demonstrated that si-Fbx32 transfection markedly reduced the protein levels of Cyclin A2, Cyclin D1, Cyclin E1, and PCNA. In contrast, co-transfection with the miR-146a-5p inhibitor counteracted this decrease,

resulting in increased protein expression (Fig. 8f-g). EdU assays demonstrated that transfection with si-Fbx32 significantly reduced the EdU-positive rate in C2C12 cells, while si-Fbx32 + miR-146a-5p I substantially increased the positivity rate (Fig. 8h-i). Transfection with si-Fbx32 notably enhanced myofiber diameter and myotubular cell nuclear fusion rate; however, these improvements were substantially reduced by co-transfection with a miR-146a-5p inhibitor (Fig. 8j-l). In C2C12 cells, si-Fbx32 transfection markedly enhanced MyoD and Pax7 fluorescence intensity, while co-transfection with a miR-146a-5p inhibitor notably decreased their intensity (Fig. 8m-p). RT-qPCR analysis revealed that si-Fbx32 transfection notably reduced the mRNA levels of the skeletal muscle atrophy markers Fbx32 and MuRF, and enhanced the mRNA expression of the skeletal muscle differentiation markers MyoD and MyoG. In contrast, the opposite results were observed in the si-Fbx32 + miR-146a-5p I group (Fig. 8q). Western blot analysis confirmed the RT-qPCR findings, showing that si-Fbx32 transfection markedly elevated skeletal muscle differentiation markers and reduced atrophy-related protein levels. The combined application of si-Fbx32 and the miR-146a-5p inhibitor reversed the alterations (Fig. 8r, Figure S5b). KEGG pathway analysis indicated that miR-146a-5p may be involved in regulating the FoxO3 signaling pathway (Figure S5a). Western blot analysis indicated a reduction in FoxO3 phosphorylation after si-Fbx32 transfection, while co-transfection with the miR-146a-5p inhibitor resulted in increased FoxO3 phosphorylation (Fig. 8r, Figure S5b). Transfection with si-Fbx32 markedly decreased the mRNA and protein expression of apoptosis and autophagy-related genes in C2C12 cells. In contrast, co-transfection with the miR-146a-5p inhibitor increased gene expression levels (Figs. 8s-t, S5c). In terms of ROS, si-Fbx32 transfection significantly lowered ROS levels and boosted ATP levels, while the si-Fbx32 + miR-146a-5p I group promoted ROS production and decreased ATP levels (Fig. 8u-w). In conclusion, this study demonstrated that miR-146a-5p modulates key biological processes like skeletal muscle cell differentiation, mitochondrial autophagy, ROS, and apoptosis by targeting the Fbx32/FoxO3 signaling pathway, offering new insights into its potential therapeutic roles in skeletal muscle diseases.

Discussion

Skeletal muscle development and maintenance decline progressively with age, a phenomenon that has been extensively validated in animal models such as pigs and mice [22–24]. The development, regulation, and maintenance of skeletal muscle function rely on multiple molecular mechanisms, notably involving miR-146a-5p [25]. sEV plays a crucial role in both normal and pathological processes, such as the maintenance and degeneration of skeletal muscle tissue [26]. MiR-146a-5p may significantly facilitate communication between adipose and skeletal muscle tissues via sEV [27]. Research consistently demonstrates a significant association between miR-146a-5p and the advancement of various diseases. miR-146a-5p is linked to muscle mass loss in postmenopausal osteoporotic women and shows increased expression in LPS-treated C2C12 myotubes, indicating its role in muscle catabolism due to acute inflammation from LPS treatment [28, 29]. MiR-146a-5p is a potential biomarker for myocardial injury in dermatomyositis and may have therapeutic potential in mitigating fibrosis following skeletal muscle damage [30, 31]. Alterations in miR-146a-5p expression during aging are closely linked to skeletal muscle atrophy development. Research indicates that aging disrupts the miR-146a-5p-regulated MMP2/16-MLCK3-p-MLC2 pathway, leading to impaired contractile function and increased heart failure risk [32]. Additionally, miR-146a-5p is recognized as a marker of cellular senescence, with its circulating levels being involved in inflammation and aging, particularly in senescent endothelial cells [33]. Research indicates that melatonin can counteract β-cell senescence induced by stearic acid by suppressing miR-146a-5p, which leads to increased Mafa expression [34–36]. Furthermore, it was discovered that senescent hepatocellular carcinoma cells suppress aerobic glycolysis by secreting exosomal miR-146a-5p, which activates the CHK2/p53/p21 signaling cascade through the targeting of IRF7, contributing to the decline of hepatocellular carcinoma cells [37]. MiR-146a-5p is involved in several biological pathways linked to skin aging, such as circadian rhythms, intercellular communication, cellular repair, cell proliferation, and collagen synthesis, positioning it as a potential target for addressing skin aging [38]. The research highlights the critical role of miR-146a-5p in the development and degeneration of skeletal muscle. Notably, its expression was significantly diminished in a senescent mouse model, exacerbating skeletal muscle atrophy and functional decline. A comparative study showed that miR-146a-5p expression increases with aging in both pigs and mice, indicating a similar regulatory pattern. Research utilizing an aKO mouse model demonstrated that miR-146a-5p deficiency impairs skeletal muscle differentiation and is associated with muscle degradation. The study highlights miR-146a-5p's crucial involvement in regulating skeletal muscle aging and atrophy. Ultimately, miR-146a-5p holds considerable significance in the aging process, as it modulates various molecular pathways that govern skeletal muscle development, deterioration, and loss of function. MiR-146a-5p offers a significant understanding of the molecular mechanisms of skeletal muscle aging and serves as a potential therapeutic target for combating age-related muscle atrophy.

In aKO mice, the deletion of miR-146a-5p led to marked skeletal muscle atrophy, along with pathological changes such as mitochondrial autophagy and apoptosis. In osteoarthritis patients, miR-146a-5p is upregulated in knee cartilage, where it negatively impacts NUMB expression, induces apoptosis, and suppresses autophagy. However, elevating NUMB levels counteracted these effects, and intra-articular delivery of a miR-146a-5p antagonist mitigated apoptotic and autophagic alterations in chondrocytes [39]. Silencing hsa-miR-146a-5p safeguarded SH-SY5Y cells against AB1-42-induced apoptosis, inhibited proliferation, and reduced autophagic vesicle accumulation [40]. Fluid shear stress-induced downregulation of miR-146a-5p alleviated osteoblast apoptosis by targeting SMAD4 [41]. In addition, miR-146a-5p attenuated adriamycin-induced cardiotoxicity through the modulation of the TAF9b/P53 pathway, thereby reducing apoptosis and regulating autophagic activity [42]. MiR-146a-5p is also involved in regulating mitochondrial RNAs, including several mRNAs, where its inhibition may disrupt mitochondrial mRNA translation due to either dysfunction of the mitochondrial ribosome or its interference with translation or cleavage processes [43]. MiR-146a-5p alleviates neuroinflammation and cognitive deficits caused by intermittent hypoxia in mice by targeting HIF1α to regulate mitochondrial ROS, influencing the secretion of NLRP3 inflammatory vesicles and inflammatory factors [44, 45]. RNA-seq analysis revealed that changes in miR-146a-5p expression are significantly linked to pathways involved in insulin secretion, apoptosis, and the regulation of mitochondrial function. In non-obese diabetic mice, the elevated levels of miR-146a-5p correlated with impaired mitochondrial activity, suggesting its potential role in β-cell damage through the inhibition of mitochondrial function [46]. In skeletal muscle, miR-146a-5p deficiency not only affects skeletal muscle development but also aggravates skeletal muscle degeneration during aging. The protective role of adipose tissue-derived miR-146a-5p on skeletal muscle, facilitated by sEV, has garnered significant interest. The study showed that injecting miR-146a-5p-enriched adipose-derived sEV into the TA muscle of aged mice significantly reduced muscle atrophy and partially enhanced muscle function, indicating a potential strategy for addressing age-related skeletal muscle degeneration. In contrast, injecting adipose-derived sEV without miR-146a-5p (aKO-sEV) not only failed to improve skeletal muscle health but also worsened skeletal muscle atrophy, with notable mitochondrial autophagy. We previously demonstrated that miR-146a-5p derived from skeletal muscle sEVs suppresses adipogenesis through the GDF5-PPARγ signaling pathway [13]. This underscores the crucial role of miR-146a-5p in maintaining the integrity and function of adipose and skeletal muscle tissues.

Fbx32, a critical E3 ubiquitin ligase associated with skeletal muscle wasting, has been implicated in promoting protein breakdown in muscle tissues under conditions such as aging, malnutrition, and various pathological states [47–51]. Our study demonstrates that miR-146a-5p mitigates skeletal muscle atrophy by directly targeting and inhibiting Fbx32 expression, underscoring its protective role against muscle degradation. By decreasing Fbx32 levels, miR-146a-5p diminishes protein breakdown in myocytes, contributing to a reduction in muscle degeneration and damage. Apoptotic signaling pathways play a crucial role in regulating protein degradation mechanisms, such as the ubiquitin-proteasome system and autophagy-lysosome pathway, during skeletal muscle atrophy [52]. MiR-146a-5p inhibited Fbx32 expression, leading to decreased mitochondrial autophagy and apoptosis, which helped maintain skeletal muscle structure and function. Targeting miR-146a-5p could potentially address aging-related skeletal muscle atrophy by regulating Fbx32. Previous research indicates that miR-146a-5p facilitates skeletal muscle differentiation and inhibits atrophy by targeting IGF1R, thereby activating the PI3K/AKT/mTOR signaling pathway [25]. This pathway is crucial for regulating muscle cell proliferation, differentiation, and metabolism, significantly contributing to muscle development and regeneration [53–55]. Research indicates that miR-146a-5p influences the PI3K/AKT/mTOR pathway via IGF1R and inhibits the FoxO3 pathway by targeting Fbx32, establishing a self-regulating feedback loop. FoxO transcription factors are closely linked to skeletal muscle atrophy, with FoxO activation promoting protein degradation and accelerating muscle functional decline [56, 57]. By suppressing FoxO activity, miR-146a-5p effectively slows skeletal muscle decline and is closely associated with mitochondrial autophagy and apoptosis. Furthermore, miR-146a-5p contributes to maintaining skeletal muscle balance by decreasing mitochondrial autophagy and apoptosis in myocytes, thus mitigating muscle wasting. MiR-146a-5p plays a vital role in preserving skeletal muscle integrity by modulating essential signaling pathways like PI3K/AKT/mTOR and FoxO, providing valuable insights for developing therapies against muscle atrophy.

Supplementary Information

The online version contains supplementary material available at https://doi.org/10.1186/s12951-025-03367-1.

Supplementary Material 1

Supplementary Material 2

Author contributions

The project was initiated by QX and JM, with MQ leading the experimental work and drafting the manuscript.MQ conducted the data collection, interpretation, and analysis. QX, JM, and MQ revised and edited the

manuscript. The other authors provided technical expertise and contributed to the result analysis, offering feedback on the manuscript.

Funding
This study was funded by the National Natural Science Foundation of China (32072814, 32072812, 32072714, 82405109), the National Science and Technology Major Project (2023ZD04068-509), the Guangdong Provincial Natural Science Foundation (2023A151502511, 2021A1515011310), the National Key Research and Development Program (2022YFC3601900), the Tianjin Municipal Education Commission Scientific Research Program (2024ZXZD001), and the Tianjin Health Science and Technology Program (TJWJ2022QN053).

Data availability
No datasets were generated or analysed during the current study.

Declarations

Ethics approval and consent to participate
All animal studies carried out under the protocols of the Animal Experimentation and Ethics Committee at Tianjin Hospital have received approval.

Consent for publication
All authors participating in this research gave their full consent to publish the findings.

Competing interests
The authors declare no competing interests.

Received: 26 February 2025 / Accepted: 1 April 2025
Published online: 10 April 2025

References

1. Scoditti E, Carpi S, Massaro M, Pellegrino M, Polini B, Carluccio MA, Wabitsch M, Verri T, Nieri P, De Caterina R. Hydroxytyrosol modulates adipocyte gene and MiRNA expression under inflammatory condition. Nutrients. 2019;11(10):2493.
2. Huang Z, Xu A. Adipose extracellular vesicles in intercellular and Inter-Organ crosstalk in metabolic health and diseases. Front Immunol. 2021;12:608680.
3. Jyoti Trivedi M, Yasir RK, Maurya. Alok Shiomurti Tripathi. Aptamer-based theranostics in oncology: design strategies and limitations. BIOI. 2024;5(1).
4. Kourembanas S. Exosomes: vehicles of intercellular signaling, biomarkers, and vectors of cell therapy. Annu Rev Physiol. 2015;77:13–27.
5. Donzelli J, Proestler E, Riedel A, Nevermann S, Hertel B, Guenther A, Gattenlöhner S, Savai R, Larsson K, Saul MJ. Small extracellular vesicle-derived miR-574-5p regulates PGE2-biosynthesis via TLR7/8 in lung cancer. J Extracell Vesicles. 2021;10(12):e12143.
6. Olie CS, Riaz M, Konietzny R, Charles PD, Pinto-Fernandez A, Kiełbasa SM, Aartsma-Rus A, Goeman JJ, Kessler BM, Raz V. Deacetylation Inhibition reverses PABPN1-Dependent muscle wasting. iScience. 2019;12:318–32.
7. Wijaya YT, Setiawan T, Sari IN, Nah SY, Kwon HY. Amelioration of muscle wasting by Gintonin in cancer cachexia. Neoplasia. 2021;23(12):1307–17.
8. Lagirand-Cantaloube J, Offner N, Csibi A, Leibovitch MP, Batonnet-Pichon S, Tintignac LA, Segura CT, Leibovitch SA. The initiation factor eIF3-f is a major target for atrogin1/MAFbx function in skeletal muscle atrophy. EMBO J. 2008;27(8):1266–76.
9. Hunt LC, Graca FA, Pagala V, Wang YD, Li Y, Yuan ZF, Fan Y, Labelle M, Peng J, Demontis F. Integrated genomic and proteomic analyses identify stimulus-dependent molecular changes associated with distinct modes of skeletal muscle atrophy. Cell Rep. 2021;37(6):109971.
10. Fanzani A, Conraads VM, Penna F, Martinet W. Molecular and cellular mechanisms of skeletal muscle atrophy: an update. J Cachexia Sarcopenia Muscle. 2012;3(3):163–79.
11. Song J, Liu J, Cui C, Hu H, Zang N, Yang M, Yang J, Zou Y, Li J, Wang L, He Q, Guo X, Zhao R, Yan F, Liu F, Hou X, Sun Z, Chen L. Mesenchymal stromal cells ameliorate diabetes-induced muscle atrophy through exosomes by enhancing AMPK/ULK1-mediated autophagy. J Cachexia Sarcopenia Muscle. 2023;14(2):915–29.
12. Mei J, Luo Z, Cai Y, Wan R, Qian Z, Chu J, Sun Y, Shi Y, Jiang Y, Zhang Y, Yin Y, Chen S. Altered atlas of Exercise-Responsive MicroRNAs revealing miR-29a-3p attacks armored and cold tumors and boosts Anti-B7-H3 therapy. Res (Wash D C). 2025;8:0590.
13. Qin M, Xing L, Wu J, Wen S, Luo J, Chen T, Fan Y, Zhu J, Yang L, Liu J, Xiong J, Chen X, Zhu C, Wang S, Wang L, Shu G, Jiang Q, Zhang Y, Sun J, Xi Q. Skeletal Muscle-Derived Exosomal miR-146a-5p inhibits adipogenesis by mediating Muscle-Fat axis and targeting GDF5-PPARγ signaling. Int J Mol Sci. 2023;24(5):4561.
14. Yu Y, Du H, Wei S, Feng L, Li J, Yao F, Zhang M, Hatch GM, Chen L. Adipocyte-Derived Exosomal MiR-27a induces insulin resistance in skeletal muscle through repression of PPARγ. Theranostics. 2018;8(8):2171–88.
15. Chen T, Song P, He M, Rui S, Duan X, Ma Y, Armstrong DG, Deng W. Sphingosine-1-phosphate derived from PRP-Exos promotes angiogenesis in diabetic wound healing via the S1PR1/AKT/FN1 signalling pathway. Burns Trauma. 2023;11:tkad003.
16. Xu Z, Fu T, Guo Q, Zhou D, Sun W, Zhou Z, Chen X, Zhang J, Liu L, Xiao L, Yin Y, Jia Y, Pang E, Chen Y, Pan X, Fang L, Zhu MS, Fei W, Lu B, Gan Z. Disuse-associated loss of the protease LONP1 in muscle impairs mitochondrial function and causes reduced skeletal muscle mass and strength. Nat Commun. 2022;13(1):894.
17. Hu T, Chang S, Qi F, Zhang Z, Chen J, Jiang L, Wang D, Deng C, Nie K, Xu G, Wei Z. Neural grafts containing exosomes derived from Schwann cell-like cells promote peripheral nerve regeneration in rats. Burns Trauma. 2023;11:tkad013.
18. Luo Z, Mei J, Wang X, Wang R, He Z, Geffen Y, Sun X, Zhang X, Xu J, Wan R, Feng X, Jiao C, Su X, Sun J, Chen S, Chen J, Mao W, Yang Y, Sun Y. Voluntary exercise sensitizes cancer immunotherapy via the collagen inhibition-orchestrated inflammatory tumor immune microenvironment. Cell Rep. 2024;43(9):114697.
19. Cao Y, Cheng K, Yang M, Deng Z, Ma Y, Yan X, Zhang Y, Jia Z, Wang J, Tu K, Liang J, Zhang M. Orally administration of cerium oxide nanozyme for computed tomography imaging and anti-inflammatory/anti-fibrotic therapy of inflammatory bowel disease. J Nanobiotechnol. 2023;21(1):21.
20. Guo W, Cai Y, Liu X, Ji Y, Zhang C, Wang L, Liao W, Liu Y, Cui N, Xiang J, Li Z, Wu D, Li J. Single-Exosome profiling identifies ITGB3 + and ITGAM + Exosome subpopulations as promising early diagnostic biomarkers and therapeutic targets for colorectal cancer. Research (Wash D C). 2023;6:0041.
21. Yang W, Ma Y, Xu H, Zhu Z, Wu J, Xu C, Sun W, Zhao E, Wang M, Reis RL, Kundu SC, Shi X, Xiao B. Mulberry Biomass-Derived nanomedicines mitigate colitis through improved inflamed mucosa accumulation and intestinal microenvironment modulation. Research (Wash D C). 2023;6:0188.
22. Bernet JD, Doles JD, Hall JK, Kelly Tanaka K, Carter TA, Olwin BB. p38 MAPK signaling underlies a cell-autonomous loss of stem cell self-renewal in skeletal muscle of aged mice. Nat Med. 2014;20(3):265–71.
23. Zhang C, Cheng N, Qiao B, Zhang F, Wu J, Liu C, Li Y, Du J. Age-related decline of interferon-gamma responses in macrophage impairs satellite cell proliferation and regeneration. J Cachexia Sarcopenia Muscle. 2020;11(5):1291–305.
24. Li L, Rozo M, Yue S, Zheng X, Tan J, Lepper F, Fan C. Muscle stem cell renewal suppressed by Gas1 can be reversed by GDNF in mice. Nat Metab. 2019;1(10):985–95.
25. Qin M, Zhu J, Xing L, Fan Y, Luo J, Sun J, Chen T, Zhang Y, Xi Q. Adipose-derived exosomes ameliorate skeletal muscle atrophy via miR-146a-5p/IGF-1R signaling. J Nanobiotechnol. 2024;22(1):754.
26. Murphy C, Withrow J, Hunter M, Liu Y, Tang YL, Fulzele S, Hamrick MW. Emerging role of extracellular vesicles in musculoskeletal diseases. Mol Aspects Med. 2018;60:123–8.
27. Qin M, Xing L, Wen S, Luo J, Sun J, Chen T, Zhang Y, Xi Q. Heterogeneity of extracellular vesicles in Porcine myoblasts regulates adipocyte differentiation. Sci Rep. 2024;14(1):26077.
28. Faraldi M, Sansoni V, Vitale J, Perego S, Gomarasca M, Verdelli C, Messina C, Sconfienza LM, Banfi G, Corbetta S, Lombardi G. Plasma MicroRNA signature associated with skeletal muscle wasting in post-menopausal osteoporotic women. J Cachexia Sarcopenia Muscle. 2024;15(2):690–701.
29. Zhang J, Fu SL, Liu Y, Liu YL, Wang WJ. Analysis of MicroRNA expression profiles in weaned pig skeletal muscle after lipopolysaccharide challenge. Int J Mol Sci. 2015;16(9):22438–55.
30. Zhang Y, Shan L, Li D, Tang Y, Qian W, Dai J, Du M, Sun X, Zhu Y, Wang Q, Zhou L. Identification of key biomarkers associated with immune cells infiltration for myocardial injury in dermatomyositis by integrated bioinformatics analysis. Arthritis Res Ther. 2023;25(1):69.

31. Sun Y, Li Y, Wang H, Li H, Liu S, Chen J, Ying H. miR-146a-5p acts as a negative regulator of TGF-β signaling in skeletal muscle after acute contusion. Acta Biochim Biophys Sin (Shanghai). 2017;49(7):628–34.
32. Dong M, Chen D, Zhu Y, Yang S, Kumar S, Zhang R, Zhou Y, Yang Z, Zheng N, Zhu T, Xiang J, Liu Y, Kang L, Liu J. Impaired regulation of MMP2/16-MLCK3 by miR-146a-5p increased susceptibility to myocardial ischaemic injury in aging mice. Cardiovasc Res. 2023;119(3):786–801.
33. Accardi G, Bono F, Cammarata G, Aiello A, Herrero MT, Alessandro R, Augello G, Carru C, Colomba P, Costa MA, De Vivo I, Ligotti ME, Lo Curto A, Passantino R, Taverna S, Zizzo C, Duro G, Caruso C, Candore G. miR-126-3p and miR-21-5p as hallmarks of Bio-Positive ageing; correlation analysis and machine learning prediction in young to Ultra-Centenarian Sicilian population. Cells. 2022;11(9):1505.
34. Nunes ADC, Weigl M, Schneider A, Noureddine S, Yu L, Lahde C, Saccon TD, Mitra K, Beltran E, Grillari J, Kirkland JL, Tchkonia T, Robbins PD, Masternak MM. miR-146a-5p modulates cellular senescence and apoptosis in visceral adipose tissue of long-lived Ames Dwarf mice and in cultured pre-adipocytes. Geroscience. 2022;44(1):503–18.
35. Su S, Zhao Q, Dan L, Lin Y, Li X, Zhang Y, Yang C, Dong Y, Li X, Regazzi R, Sun C, Chu X, Lu H. Inhibition of miR-146a-5p and miR-8114 in Insulin-Secreting cells contributes to the protection of melatonin against stearic Acid-Induced cellular senescence by targeting Mafa. Endocrinol Metab (Seoul). 2022;37(6):901–17.
36. Lei Q, Liu T, Gao F, Xie H, Sun L, Zhao A, Ren W, Guo H, Zhang L, Wang H, Chen Z, Guo AY, Li Q. Microvesicles as potential biomarkers for the identification of senescence in human mesenchymal stem cells. Theranostics. 2017;7(10):2673–89.
37. Yang S, Li A, Lv L, Zheng Z, Liu P, Min J, Wei J. Exosomal miRNA-146a-5p derived from senescent hepatocellular carcinoma cells promotes aging and inhibits aerobic Glycolysis in liver cells via targeting IRF7. J Cancer. 2024;15(14):4448–66.
38. Stafa K, Rella A, Eagle W, Dong K, Morris K, Layman D, Corallo K, Trivero J, Maidhof R, Goyarts E, Pernodet N. miR-146a is a critical target associated with multiple biological pathways of skin aging. Front Physiol. 2024;15:1291344.
39. Zhang H, Zheng W, Li D, Zheng J. miR-146a-5p promotes chondrocyte apoptosis and inhibits autophagy of osteoarthritis by targeting NUMB. Cartilage. 2021;13(2suppl):S1467–77.
40. Fan Y, Zhang J, Zhuang X, Geng F, Jiang G, Yang X. Epigenetic transcripts of LINC01311 and hsa-miR-146a-5p regulate neural development in a cellular model of Alzheimer's disease. IUBMB Life. 2021;73(7):916–26.
41. Liu X, Zhang K, Wang L, Geng B, Liu Z, Yi Q, Xia Y. Fluid shear stress-induced down-regulation of miR-146a-5p inhibits osteoblast apoptosis via targeting SMAD4. Physiol Res. 2022;71(6):835–48.
42. Pan JA, Tang Y, Yu JY, Zhang H, Zhang JF, Wang CQ, Gu J. miR-146a attenuates apoptosis and modulates autophagy by targeting TAF9b/P53 pathway in doxorubicin-induced cardiotoxicity. Cell Death Dis. 2019;10(9):668.
43. Dasgupta N, Peng Y, Tan Z, Ciraolo G, Wang D, Li R. MiRNAs in mtDNA-less cell mitochondria. Cell Death Discov. 2015;1:15004.
44. Zhang Y, Miao Y, Xiong X, Tan J, Han Z, Chen F, Lei P, Zhang Q. Microglial exosomes alleviate intermittent hypoxia-induced cognitive deficits by suppressing NLRP3 inflammasome. Biol Direct. 2023;18(1):29.
45. Guo Z. Phei Er saw and Sangyong Jon. Non-Invasive physical stimulation to modulate the tumor microenvironment: unveiling a new frontier in cancer therapy. BIOI. 2024;5(1).
46. Krishnan P, Branco RCS, Weaver SA, Chang G, Lee CC, Syed F, Evans-Molina C. miR-146a-5p mediates inflammation-induced B cell mitochondrial dysfunction and apoptosis. J Biol Chem. 2024;300(11):107827.
47. Lee K, Jin H, Chei S, Oh HJ, Lee JY, Lee BY. Effect of dietary silk peptide on obesity, hyperglycemia, and skeletal muscle regeneration in High-Fat Diet-Fed mice. Cells. 2020;9(2):377.
48. Clifford T. Nutritional and Pharmacological interventions to expedite recovery following Muscle-Damaging exercise in older adults: A narrative review of the literature. J Aging Phys Act. 2019;27(4):914–28.
49. Lee SY, Tung HH, Liu CY, Wei J, Chen LK. Corrigendum to 'tangible dynamic changes in resilience, nutrition, and leisure activity of older patients with cardiovascular disease and possible sarcopenia: A longitudinal study' [Archives of Gerontology and Geriatrics AGG, 91, July-August 2021, 104416]. Arch Gerontol Geriatr. 2021;96:104456.
50. Lin X, Smith C, Moreno-Asso A, Zarekookandeh N, Brennan-Speranza TC, Duque G, Hayes A, Levinger I. Undercarboxylated osteocalcin and ibandronate combination ameliorates hindlimb immobilization-induced muscle wasting. J Physiol. 2023;601(10):1851–67.
51. Belghit I, Skiba-Cassy S, Geurden I, Dias K, Surget A, Kaushik S, Panserat S, Seiliez I. Dietary methionine availability affects the main factors involved in muscle protein turnover in rainbow trout (Oncorhynchus mykiss). Br J Nutr. 2014;112(4):493–503.
52. Zhang W, Sun W, Gu X, Miao C, Feng L, Shen Q, Liu X, Zhang X. GDF-15 in tumor-derived exosomes promotes muscle atrophy via Bcl-2/caspase-3 pathway. Cell Death Discov. 2022;8(1):162.
53. Kim JH, Choi TG, Park S, Yun HR, Nguyen NNY, Jo YH, Jang M, Kim J, Kim J, Kang I, Ha J, Murphy MP, Tang DG, Kim SS. Mitochondrial ROS-derived PTEN oxidation activates PI3K pathway for mTOR-induced myogenic autophagy. Cell Death Differ. 2018;25(11):1921–37.
54. Qian Z, Ye J, Li J, Che Y, Yu W, Xu P, Lin J, Ye F, Xu X, Su Z, Li D, Xie Z, Wu Y, Shen H. Decrotonylation of AKT1 promotes AKT1 phosphorylation and activation during myogenic differentiation. J Adv Res. 2023;50:117–33.
55. Wuputra K, Ku CC, Wu DC, Lin YC, Saito S, Yokoyama KK. Prevention of tumor risk associated with the reprogramming of human pluripotent stem cells. J Exp Clin Cancer Res. 2020;39(1):100.
56. Willis MS, Schisler JC, Portbury AL, Patterson C. Build it up-Tear it down: protein quality control in the cardiac sarcomere. Cardiovasc Res. 2009;81(3):439–48.
57. Abdesselam I, Dutour A, Kober F, Ancel P, Bege T, Darmon P, Lesavre N, Bernard M, Gaborit B. Time course of change in ectopic fat stores after bariatric surgery. J Am Coll Cardiol. 2016;67(1):117–9.

Publisher's note